SCIENCE CHINA
Earth Sciences

• REVIEW •

September 2014 Vol.57 No.9: 1995–2012
doi: 10.1007/s11430-014-4923-3

Recent investigation on the coupling between the ionosphere and upper atmosphere

WAN WeiXing[1*] & XU JiYao[2]

[1] *Key Laboratory of Earth and Planetary Physics, Institute of Geology and Geophysics, Chinese Academy of Sciences, Beijing 100029, China;*
[2] *State Key Laboratory of Space Weather, Center for Space Science and Applied Research, Chinese Academy of Sciences, Beijing 100190, China*

Received March 14, 2014; accepted May 26, 2014; published online July 22, 2014

Scientific attention has recently been focused on the coupling of the earth's upper atmosphere and ionosphere. In the present work, we review the advances in this field, emphasizing the studies and contributions of Chinese scholars. This work first introduces new developments in the observation instruments of the upper atmosphere. Two kinds of instruments are involved: optical instruments (lidars, FP interferometers and all-sky airglow imagers) and radio instruments (MST radars and all-sky meteor radars). Based on the data from these instruments and satellites, the researches on climatology and wave disturbances in the upper atmosphere are then introduced. The studies on both the sporadic sodium layer and sporadic E-layer are presented as the main works concerning the coupling of the upper atmosphere and the low ionosphere. We then review the investigations on the ionospheric longitudinal structure and the causative atmospheric non-migrating tide as the main progress of the coupling between the atmosphere and the ionospheric F2-region. Regarding the ionosphere-thermosphere coupling, we introduce studies on the equatorial thermospheric anomaly, as well as the influence of the thermospheric winds and gravity waves to the ionospheric F2-region. Chinese scholars have made much advancement on the coupling of the ionosphere and upper atmosphere, including the observation instruments, data precession, and modeling, as well as the mechanism analysis.

upper atmosphere, ionosphere, vertical coupling

Citation: Wan W X, Xu J Y. 2014. Recent investigation on the coupling between the ionosphere and upper atmosphere. Science China: Earth Sciences, 57: 1995−2012, doi: 10.1007/s11430-014-4923-3

The variability of the ionosphere includes space weather variations having short time scales and space climatology having long periods. It is well known that the ionospheric variability is mainly driven by solar activities, disturbances of the solar wind and magnetosphere, and atmospheric waves propagated from the lower atmosphere (Robert and Pfaff, 2012). The observations indicated that these three types of external sources contribute almost equally to the variations of the ionosphere (Forbes et al., 2000; Rishbeth and Mendillo, 2001; Rishbeth, 2006).Thus, the disturbances from the lower atmosphere and from ground surface must be considered as one of the most important sources of ionospheric space weather and space climate.

Ionospheric responses to atmospheric waves involve the vertical couplings in the atmosphere-ionosphere system, which is a hot field in the study of aeronomy. The International Association of Geomagnetism and Aeronomy subordinates (IAGA), an affiliated agency of the International Union of Geodesy and Geophysics (IUGG), organized a number of workshops and published three special issues of *Journal of Atmospheric and Solar-Terrestrial Physics* (Pancheva et al., 2006, 2007, 2012), along with amonograph (Abdu et al., 2011). The Scientific Committee on Solar-Terrestrial Physics (SCOSTEP) has sponsored an international program 'Climate And Weather of the Sun-Earth

*Corresponding author (email: wanw@mail.iggcas.ac.cn)

System (CAWSES, CAWSES-II),' in which the special working group (TG4) is devoted to study the responses of the geospace to the lower atmosphere (Schmieder et al., 2004; Basu and Pallamraju, 2006).

In the atmosphere-ionosphere system, various activities in the lower atmosphere, such as the absorption of the solar UV radiation by the stratospheric ozone, severe weather events in the troposphere, and the interaction between the troposphere and the terrestrial topography, result in a variety of disturbances in the near earth space. The released energy propagates upward in the forms of gravity waves, tides, and planetary waves. When the atmospheric waves propagate upward, their amplitudes tend to increase to conserve the wave energy density due to the decrease of the background density. On the other hand, wave amplitudes decay rapidly with height above the bottom thermosphere due to the rapid increase of the background temperature. This, in turn, induces the increase of atmospheric molecular viscosity and thermal conductivity. As a result, most of the wave energy can only be transmitted to the mesosphere and lower thermosphere (MLT).

Both observational and the theoretical studies have shown that the coupling of the upper atmosphere and ionosphere has the following forms: (1) Atmospheric waves in the MLT region interact with the nearby lower ionosphere. For instance, in the ionospheric E region at mid-latitudes, the wind shear leads to metalions accumulating, resulting in the sporadic E layer. (2) Part of the wave energy may propagate, or leak, into the upper thermosphere/ionosphere F2-region, then creating wave-like variations of the plasma density through the neutron-ion collisions. This may further excite ionospheric irregularities due to the plasma instabilities in the low latitude and equatorial regions. (3) At mid-latitudes, the atmospheric waves in the MLT region drive the motions of charged particles, which cross the geomagnetic field lines and generate electric fields through the ionospheric dynamo effect. Along the magnetic field lines, these electric fields can map into the F2-layer over the equatorial and low latitude regions. This in turn causes the plasma drift and redistribution to form the equatorial ionospheric anomalies.

In recent years, significant progress has been made in the investigation of coupling of the upper atmosphere and ionosphere, mainly due to the rapid development of upper atmospheric observations. The GUVI, SABER and TIDI instruments onboard the TIMED satellite have worked for nearly a solar cycle (~11 years) to measure the global atmospheric temperature, density, composition and wind in the MLT region with considerably high precision (Yee et al., 1999; Christensen et al., 1994; Russell et al., 1999; Killeen et al., 1999, 2005). The CHAMP and GRACE satellites also performed long-term observations on the wind and density in the upper thermosphere (Reigber et al., 2002; Guo et al., 2007; Liu H X et al., 2007). These space-borne observations have significantly contributed to recent research of upper atmospheric dynamics. In terms of ground-based observations, both the optical (e.g., lidar) and radio (e.g., all-sky meteor radar) instruments have made great progress. Using instruments, a large number of datasets for the atmospheric parameters have been obtained in the MLT and the upper thermosphere region (Gardner and Voelz, 1987; She et al., 1992; Yu J Y and She, 1993; Gong S S et al., 2003; Yu Y et al., 2013). As a result of these observations scientists have extensively studied the propagation, attenuation and nonlinear effects of gravity waves, tides, and planetary waves and their ionosphere responses, as well as the couplings of the thermosphere and ionosphere.

Following the success of the international research on the coupling of the upper atmosphere and ionosphere, Chinese scientists have also made significant achievements in observational and scientific research. This review paper focuses mainly on Chinese scientists' recent research, emphasizing the works on the upper the atmosphere (one can refer to Liu L B et al. (2011) for the review on the investigation of the ionosphere).

1 Upper atmosphere observations

It is well known that observation plays a key role in studying the coupling between the upper atmosphere and ionosphere. Ionospheric observations have a long history and have evolved. However, a lack of observations of the upper atmosphere limited the previous studies for the coupling of upper atmosphere and ionosphere. In recent years, the observational technique for the upper atmosphere has been developed rapidly. In the observation using space-borne techniques, the Thermosphere-Ionosphere-Mesosphere Energetics and Dynamics (TIMED) satellite carried a series of instruments for the upper atmospheric observations (Yee et al., 1999). These instruments include the Global Ultra-violet Imager (GUVI), designed to measure the atmospheric composition and temperature of the lower thermosphere (Christensen et al., 1994). Another instrument is the Sounding of the Atmosphere using Broadband Emission Radiometry (SABER), which provides the vertical profiles of kinetic temperature, pressure, geopotential height, volume mixing ratios for the trace species, and volume emission rates (Russell et al., 1999). A third instrument is the TIMED Doppler Interferometer (TIDI), used to measure the vector winds in the MLT region (Killeen et al., 1999, 2005). The accelerometers mounted on CHAMP, GRACE, etc., are able to carry in-situ measurements of the thermospheric wind and density (Sutton et al., 2007). These on-board instruments have provided long-term global high-resolution observations for the atmospheric temperature, density and wind in the MLT and thermosphere. They have also advanced our understanding of the fundamental processes governing the energetics, chemistry, dynamics and transport in the upper atmosphere.

The ground-based optical technique for observing the upper atmosphere has also been developed rapidly, and this includes the upper atmospheric lidar, Fabry-Pérot (FP) interferometer and the all-sky airglow imager. The upper atmospheric lidar issued to measure the temperature, the wind in the stratosphere, mesosphere and lower-thermosphere, as well as the metal atoms/ions in the MLT (Gardner and Voelz, 1987; She et al., 1992; Yu and She, 1993). The FP interferometers can observe the wind in the thermosphere (~250 km) and the MLT region (~87 km, ~97 km) (Niciejewski et al., 1994; Wu et al., 2004). The all-sky airglow imagers are used to obtain the horizontal structure of the OH and OI (green line) airglow emissions in the mesopause region as well as the OI (red line) airglow emission in the thermosphere (~250 km) (Peterson and Kieffaber, 1973; Peterson, 1979; Taylor, 1997). On the other hand, the ground-based radio technique for detecting the upper atmosphere is becoming more and more mature and is applied widely. For example, the worldwide all-sky meteor radars, the mesosphere-stratosphere-troposphere (MST) radars, have provided a large amount of wind observations in the MLT region.

In recent years, the ground-based observations in China have grown fast, especially with support from "the Meridian Project". In fact, 28 series of upper atmospheric observational instruments have been set up at 15 observatories (ref. Table 1).

Upper atmospheric lidar development in China began at the end of the twentieth century. Gong et al. (1997) built the first broadband Na lidar to measure the sodium density in the region of 80–110 km over Wuhan in China. Later, Gong et al. (2003) developed a dual-band Rayleigh-Na lidar, which is able to detect the atmospheric temperature/density in the height range of 30–70 km and the sodium density in the height range of 80–110 km simultaneously. They also developed the technique for measuring sodium density during the daytime. The lidar group at Wuhan University (WHU) built a series of lidars, e.g., Na lidar, Fe lidar, and Ca/Ca^+ lidar. These three independent resonance fluorescence lidars allow for simultaneous and nearly common-volume measurements of three metal species (Na, Fe and Ca or Na, Fe and Ca^+) (Yi et al., 2008, 2009; Chen and Yi, 2011).

Based on the construction of a Rayleigh-Na lidar, the group at the University of Science and Technology of China (USTC) has given priority to the development of wind lidars. They built the first stratospheric Doppler wind lidar in China, which is based on a double-edged technique and is able to measure the wind up to 40 km (Xia et al. 2012; Shu et al. 2012). Recently, the USTC group successfully developed

Table 1 The upper atmospheric observatories and the instruments in China

Observatory	Location	Instruments	Paramters[a)]	Altitude (km)	Division
Mohe	53.5°N, 122.3°E	Meteor radar	*U*, *V*, *T*	75–110	IGGCAS
Xinglong	40.4°N, 117.6°E	FP interferometer	*U*, *V*, *T*	87, 94, 250	CSSAR
		Airglow imager	{OH}, {O}	87, 94, 250	
Yanqing	40.2°N, 116.2°E	Rayleigh-Na lidar	*T*, ρ, [Na]	30–70, 80–110	CSSAR
Langfang	39.5°N, 116.7°E	Narrow-band Na lidar	ρ, [Na]	80–110	CSSAR
		Airglow imager	{OH}	87	
		MF radar	*U*, *V*	80–100	
Beijing	40.3°N, 116.2°E	Meteor radar	*U*, *V*, *T*	75–110	IGGCAS
Xianghe	39.8°N, 116.9°E	MST radar	*U*, *V*	10–40, 70–120	IAPCAS
Kelan	38.7°N, 111.6°E	FP interferometer	*U*, *V*, *T*	250, 97, 87	NCSW
Wuzhai	38.9°N, 111.8°E	MF radar	*U*, *V*	60–100	NCSW
Qingdao	36.0°N, 120.2°E	Na lidar	ρ, [Na]	80–100	CIRWP
Hefei	31.8°N, 117.3°E	Raleigh-Na lidar	*T*, ρ, [Na]	30–70, 80–110	USTC
		Wind lidar	*U*, *V*	0–60	
		Narrow-band Na lidar	*T*, *U*, *V*, [Na]	80–105	
		Airglow imager	{OH}, {O}	87, 94, 250	
Wuhan	30.5°N, 114.4°E	Na lidar	*T*, ρ, [Na]	30–70, 80–110	WHU
		Fe lidar	*T*, [Fe]	0–70, 80–110	
		Ca/Ca^+ lidar	[Ca], [Ca^+]	80–110	
		MST radar	*U*, *V*	10–40, 70–120	
Wuhan	30.5°N, 114.4°E	Rayleigh-Na lidar	*T*, ρ, [Na]	30–70, 80–110	WIPM
Wuhan	30.5°N, 114.4°E	Meteor radar	*U*, *V*, *T*	75–110	IGGCAS
Qujing	25.6°N, 103.8°E	Meteor radar	*U*, *V*, *T*	75–110	CIRWP
		MF radar	*U*, *V*	60–100	
Qujing	25.6°N, 103.8°E	Airglow imager	{OH}, {O}	87, 94, 250	CSSAR
Haikou	20.0°N, 110.4°E	Raylegih-Na lidar	*T*, ρ, [Na]	30–70, 80–110	CSSAR
Fuke	19.5°N, 109.1°E	Meteor radar	*U*, *V*	80–100	CSSAR
		Airglow imager	{OH}, {O}	87, 94, 250	
Sanya	18.3°N, 109.6°E	Meteor radar	*U*, *V*, *T*	75–110	IGGCAS

a) *U*: zonal wind; *V*: meridional wind; *T*: temperature; ρ: atmospheric density; [x]: metal atoms/ions density; {x}: airglow density.

a mobile Doppler wind lidar constructed with three independent large-aperture (1-m diameter) lidar systems. They extended the wind measurement to approximately 60 km, as shown in Figure 1. Additionally, the USTC group built a narrow-band Na lidar, which can measure wind, temperature and sodium density in the height range of 80–110 km simultaneously (Li T et al., 2012a).

Supported by the Chinese "Meridian Project", four Rayleigh-Na lidars have been built in Beijing, Hefei, Wuhan and Haikou by the Center for Space Science and Applied Research (CSSAR), USTC and WHU, respectively. A lidar chain has thus formed and is used to observe the atmospheric density between 30–70 km and sodium density between 80–110 km (Wang et al., 2012; Gong S H et al., 2013). Moreover, the Chinese Institute of Radio Wave Propagation (CIRWP) also built a Na lidar in Qingdao.

In addition to the above lidars, two FP interferometers have been built at Xinglong and Kelan by CSSAR and the National Center for Space Weather (NCSW), respectively. These are used to detect the wind in thermosphere (~250 km) and the MLT (~87 km, ~94 km) (Yuan et al., 2010, 2013; Jiang et al., 2012). CSSAR has also developed all-sky airglow imagers both in Xinglong and Langfang. The airglow imagers provide the horizontal structure of the OH airglow emission near the mesopause region, which is used to retrieve the characteristics of gravity waves at the corresponding altitudes (Tu et al., 2009; Li Q et al., 2011, 2013). CSSAR has also developed and installed a Spectrometer of atmospheric radiation at Xinglong Station, used to obtain the rotational temperature through the OH radiation spectrum (Zhu et al., 2012).

The Chinese "Meridian Project" also developed radio observational instruments in China. The Institute of Atmosphere Physics, Chinese Academy of Sciences (IAPCAS) and WHU collaboratively built two MST radars in Xianghe and Wuhan, respectively. The MST radar measures the horizontal wind in the troposphere, stratosphere (10–45 km) and mesosphere regions through radar signals returned from refractive index fluctuations produced by turbulence in the neutral atmosphere and the strong vertical gradient in electron density.

The all-sky meteor radar is the most effective way to detect the wind in the MLT region as it measures the Doppler shift and arriving angle of the echoes (~30 MHz), which are scattered by meteor trails in the MLT region. The meteor radar can also be used to estimate the background atmospheric temperature through the decay time of the radar signals. Today, the meteor radar has become the most popular instrument for measuring the upper atmosphere. The first meteor radar in China was built in Wuhan in 2001. After a three-year observation, a series of works were published to characterize the mean wind and tides over Wuhan (Xiong et al., 2004; Niu et al., 2005; Zhao et al., 2005a, 2005b). Recently, the Institute of Geology and Geophysics, Chinese Academy of Sciences (IGGCAS) has established a meridian meteor radar chain, which includes four all-sky meteor radars in Mohe, Beijing, Wuhan and Sanya. This chain across the middle and low latitudes in the northern hemisphere, to measure the wind as well as the background temperature at altitudes from 70 to 110 km. Based on the observations from the meteor radar chain, Yu et al. (2013) mapped the horizontal wind in the domains of latitude, altitude and local time along 120°E meridian using the classical atmospheric tidal theory. Additionally, the CIRWP also built an all-sky meteor radar in Qujing.

MF radars have also been built in Qujing, Langfang, and Wuzhai by CIRWP, CSSAR and NCSW, respectively. The MF radar measures the wind of 60–100 km via the scattered echoes of ionospheric irregularities.

2 Variability of the upper atmosphere

The upper atmospheric variability, including the wave

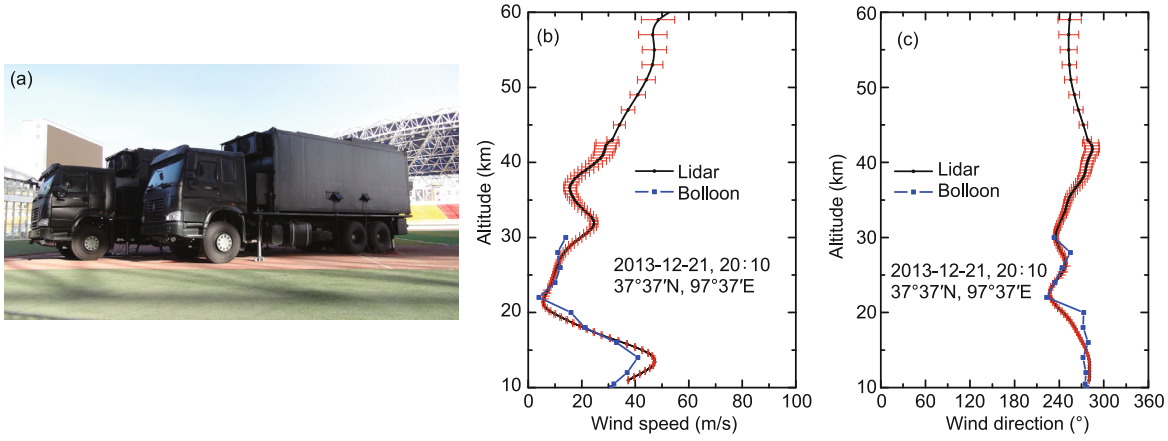

Figure 1 The Doppler wind lidar developed by USTC group (a). The center and right panels show the wind velocity (b) and direction (c) obtained by the lidar system and comparison with the measurements of balloon (blue lines) on Dec. 21, 2013 at Qinghai. Provided by Dou XianKang (2014, private communication).

perturbations and the long-term background variations, plays an important role in the coupling between the upper atmosphere and ionosphere. The seasonal and inter-annual variations of the background parameters (e.g., neutral density, temperature and wind) have been extensively studied based on satellite and ground observations, as well as atmospheric general circulation model (Garcia et al., 1997; Leblanc et al., 1998). Chinese scientists have made significant contribution to this field.

Dou et al. (2009a) studied, in detail, the semiannual oscillation (SAO) and annual oscillation (AO) in temperatures between 20 and 80 km in the middle latitude of the northern hemisphere. Dou et al. (2009b) used long-term lidar night time observations and SABER temperature observations. Figure 2 shows the comparison of the monthly mean temperature AO and SAO observed by the lidar and SABER, as well as the tide amplitude AO and SAO observed by SABER in southern California (34°N). The clear differences are observed in the middle layer between ground-based and space-born observations, and this is due to the strong AO in the diurnal amplitude. The results suggested that the diurnal tide has a significant impact on the nighttime temperatures in the upper mesosphere. In addition, Li T (2011) studied the long-term trend and solar cycle variation of the mesosphere and stratosphere from the observation of a Rayleigh lidar.

Using the TIMED/SABER temperature observations, Xu et al. (2006a, 2007a, 2007b) studied the global temperature structure, along with the properties of the AO, SAO and the quasi-biennial oscillation (QBO) in the in the mesopause region. They also investigated the mesospheric responses to the solar activity. Gan et al. (2012) reveaed the lower mesospheric inversion layers at low and middle latitudes. Li T et al. (2008) studied the QBO phenomenon, the upper atmospheric response temperature to the El Niño Southern Oscillation (ENSO) and the 11-year solar activity cycle with a 14-year lidar data set. Li T et al. (2013) further studied the mechanisms of the hemispheric coupling of the upper atmosphere from a 11-year observation period through the TIMED/SABER satellite during the ENSO events, augmented by a 53-year period model resulting from the Whole Atmosphere Community Circulation Model (WACCM), developed by National Center for Atmospheric Research (NCAR).

The upper atmospheric variability also concerns the propagation of the gravity waves (Fritts and Alexander, 2003), tides (Chapman and Lindzen, 1970) and planetary waves (Andrews et al., 1987), as well as their dissipation and nonlinear interaction (Lindzen, 1981; Holton, 1982; Holton and Alexander, 2000).

In the studies of the upper atmospheric gravity waves, Dou et al. (2010b) analyzed a five-year data set of the all-sky OH airglow imager located over northern Colorado. They studied the seasonal variations of the propagation direction and found that the gravity waves tend to propagate polar ward and equatorward in the summer and winter, respectively. This is possibly related to the gravity waves that are generated through deep convection at low latitudes in the summer and ducted waves induced by storms and fronts at high latitudes in the winter. Tang et al. (2014) quantitatively calculated the gravity wave momentum flux with both the OH all-sky imager dataset and the nearby MF radar. They found that the momentum flux of the gravity waves is significantly modulated by tides, and both the propagation direction and the momentum flux of the waves change dramatically before and after stratospheric warming events. Li Q et al. (2011) statistically studied the seasonal variations of gravity waves in the upper atmosphere with OH imager observations at Xinglong Station. The results show that the gravity waves propagate southwest in the winter and northeast in the summer, with no significant orientation in spring and autumn. This is likely related to the gravity wave filtering effect of the background winds. In addition, the gravity wave-breaking in the upper mesosphere directly drives or

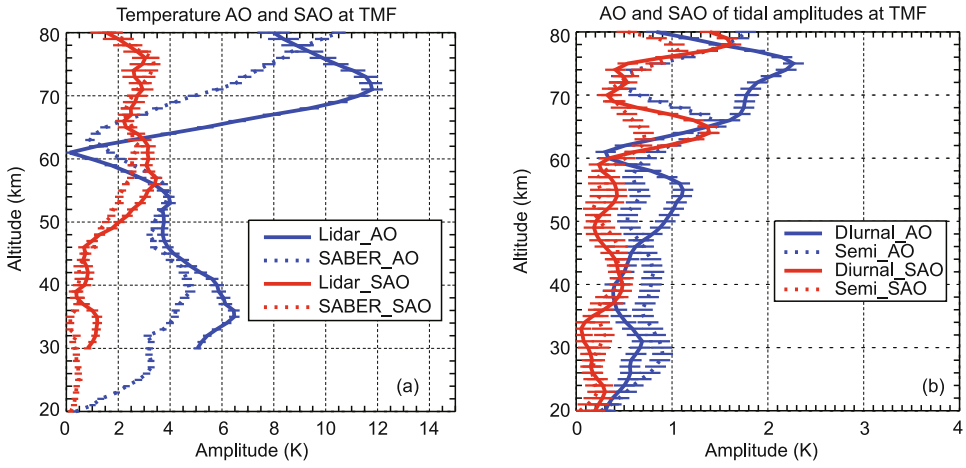

Figure 2 Observations of the amplitudes of the temperature AO and SAO (a) and the amplitudes of the AO and SAO in tide amplitude (b). After Dou et al. (2009a).

changes the structure of the background atmosphere and the distributions of the turbulence (Xu et al, 2009b; Li T et al, 2007, 2010, 2012b). From the TIMED/SABER observation of global atmospheric temperature, Zhang Y et al. (2012) studied temporal and spatial distribution of the stratospheric gravity waves as well as the corresponding wave sources. Wu and Xu (2006) investigated the vertical wave number spectra of the gravity waves derived from chaff rockets. Further, Using temperature profiles from TIMED/SABER and wind profiles from the meteor radar, Li Q et al. (2013) studied the generation mechanisms of the bore event and its influences on Na density at Xinglong Station.

The study of the gravity wave characteristics in the lower atmosphere is important to understand wave propagation and dissipation in the upper atmosphere, since most of the wave sources are located in the lower atmosphere. Zhang S D et al. (2010, 2012, 2013) studied the characteristics of the gravity waves and the inertial gravity wave parameters (e.g., period, wave speed and vertical wavelength) in the lower atmosphere with radiosonde observations. Moreover, the latitudinal, vertical and seasonal variations of the inertial gravity waves were also investigated. Chen et al. (2012) utilized the WRF model to simulate the gravity waves and the propagations generated by tropical cyclones. Huang K M et al. (2009, 2010, 2013a) simulated gravity waves under nonlinear resonance conditions and found it may be significant in the gravity wave spectral distribution in the upper atmosphere. Liu X et al. (2009) simulated Kelvin-Helmholtz instability of gravity waves and its effect on the mean flow by using a high resolution numerical model.

For the tide studies, Xue et al. (2007, 2008) analyzed the diurnal and semidiurnal tide over Wuhan with a meteor radar wind dataset and using the canonical correlation analysis (CCA) method. They found that the tidal variations are directly modulated by the seasonal variations, the solar rotation period (~27 days) and planetary waves. Using the data observed by meteor radars recently built in Mohe, Beijing, Wuhan and Sanya along the 120°E meridional line, Yu et al. (2013) obtained the two-dimensional tidal distributions at middle and low latitudes in the northern hemisphere using the classical Hough mode decomposition method. The meteor radar wind observations over Maui (20.75°N, 156.43°W) showed evidence of an 8-hour tidal component with significant semiannual variations (Jiang et al., 2009). In addition, Jiang et al. (2010) analyzed the meteor radar wind observations in Hainan and presented the diurnal and semidiurnal tidal variations in the low latitude upper atmosphere. Furthermore, Zhao et al. (2012) studied the vertical and seasonal variations of the diurnal and semidiurnal tidal variations through MF radar observations at Qujing Station.

Xu et al. (2009a) extracted the zonal mean and migrating tidal variations of the temperature, pressure and wind fields with TIMED satellite observations. They also extracted their global distribution and seasonal and quasi biennial oscillations. Xu et al. (2009b) then reported the seasonal variations and the global distribution of the atmospheric eddy coefficient by introducing the equivalent Rayleigh dissipation factor and TIMED/TIDI wind observations. The global distributions and seasonal variations of the 24-, 12-, 8- and 6-hour tidal sources are investigated by Xu et al. (2010a, 2012a), who further analyzed stratosphere ozone heating. On the basis of satellite observations, Xu et al. (2010b) found that the atmospheric airglow is strongly modulated by migrating and non-migrating tides, and Xu et al. (2012b) studied the radiation mechanism of the atmospheric airglow. Using the TIMED/SABER satellite temperature observations, Chen and Lü (2009) studied the propagation DE3 tide in the upper atmosphere.

Jiang et al. (2008) comprehensively studied a strong 6.5-day wave during April and May of 2003 with six radar observations at middle and low latitude regions. Recently, Gu et al. (2013a) and Huang Y Y et al. (2013) investigated the seasonal and inter-annual variations of the quasi-two-day wave from 20 to 120 km using the 11-year TIMED satellite temperature and horizontal wind observations. The results showed significant inter-annual variations for both $s=-3$ and $s=-4$ QTDW modes, which is related to the summer easterly jet strength and could also be modulated by the sudden warming and solar activities of the winter stratosphere. In addition, the 16-year mesosphere wind observations through Hawaii MF radar showed that the amplitudes of QTDW are strongly correlated with the 11-year solar cycle and affected by the ENSO (Gu et al. 2013b). Gan et al. (2012) studied the $s=1$ quasi-stationary and the 16-day planetary waves and their effects on the temperature inversion in the mesosphere.

In the field of wave-wave interactions, Li T et al. (2009) studied the short-term variability of the diurnal and semidiurnal tides with temperature/wind obtained by the sodium lidar observations. They showed that the tidal wave amplitudes and phases changed dramatically on a day-to-day basis, and these are closely related to the propagation directions and the strength of gravity waves observed by a collocated all-sky airglow imager. Simulation results also showed that the nonlinear interactions between gravity waves and tides could effectively affect the day-to-day variability of the tidal amplitudes (Liu X et al., 2008). Simulations by Huang C M et al. (2013) indicate that the variation of the tidal winds may change the frequency of the gravity waves; this leads to the penetration of the gravity waves to the critical layer associated with the tidal winds. Liu X et al. (2012, 2013) also pointed out that the non-isothermal background atmosphere may affect the vertical propagation of the gravity waves and change their vertical wavelengths. Further, the nonlinear interactions between quasi-stationary planetary waves and the migrating tides can generate strong non-migrating tides, which lead to dramatic changes in the short-term tidal amplitudes that have been observed by ground-based instruments (Liu and Hagan, 1998). Through satellite observations, Xu J Y et al. (2014) showed strong

evidence of the nonlinear interactions between migrating diurnal tides and planetary waves, which is suggested to be an important source of the non-migrating diurnal tides. The nonlinear interactions between quasi two-day waves and tides were observed by Huang K M et al. (2013b) through meteor radar wind observations in Hawaii. These generated two planetary waves with periods of 16.2 and 15.8 hours. Huang C M et al. (2012) analyzed the tides and planetary waves in the thermosphere wind field through Arcebo incoherent scatter radar. The results showed that the tides dominate the day-to-day variations in the thermosphere, accompanied by strong gravity waves, tides and planetary wave interactions. The nonlinear interaction between tides and planetary waves was also investigated by Huang C M et al. (2009), Gong Y et al. (2011, 2013) and Huang K M et al. (2013c). In addition, Huang K M et al. (2012) studied the nonlinear interaction of gravity waves with a two-dimensional model.

3 The coupling of the upper atmosphere, metal layers and the lower ionosphere

The mesopause is the most complex part of the atmospheric dynamical and chemical processes, as well as the critical coupling region of the upper atmosphere and ionosphere. Extraterrestrial material is deposited in this region, giving rise to layers of free metal atoms or ions (e.g., Na, Fe, Ca, Ca^+) in the MLT from 80 to 105 km. The metal atoms/ ions can be deemed a positive tracer of the atmospheric dynamical and chemical processes; thus, many researchers have paid more attention to studies that focus on the metal layers. Since the 1970s, fluorescence lidars have been used to detect the metal layers in the MLT. One of the most interesting features in the metal layers is the sporadic metal layer, which is defined as an abrupt increase in the metal density relative to the background level. On the other hand, in the mid-latitude, the metal ions in the ionospheric E-region can be converged into a narrow layer by the vertical shear of the background horizontal wind, causing the so-called sporadic E (Es) layers. The high correlation in time and space between the sporadic metal layer and Es is evidence of interpreting the mechanisms of the sporadic metal layer.

Since the 1950s, the mid-latitude Es layer has been widely investigated to study its occurrence, distributions, generation mechanism, etc. However, some observational features of Es remain uncovered, one of which is the so-called "summer anomaly" (the occurrence of mid-latitude Es is extremely high during summer). The well-known explanation of mid-latitude Es is that the wind shear mechanism is directly affected by the atmospheric waves. Thus, in recent years, researchers have tried to investigate the relationship between the "summer anomaly" of Es and the seasonal variations of the atmospheric waves. Zuo and Wan (2008) revealed the quasi 6-day oscillations in Es occurrence, which relates the quasi 6-day planetary wave activity in the MLT region. They used observations of both the ionosonde and meteor radar located at Wuhan. Later, by analyzing the observations from several worldwide ionosonde stations, Zuo et al. (2009) found the global 6-day planetary wave oscillations detected in the Es layer propagated westward with a zonal wave number of about 1. Zhao et al. (2008) studied the anomalous enhancement of ionospheric electron content in the Asian-Australian region during a geomagnetically quiet day and found a large increase of Es prior to the start of an anomalous enhancement. The day-to-day variability of Es suggested that the enhancement process was related to the lower atmospheric 2-day waves. The confirmation of the relationship between the atmospheric waves and ionospheric Es proposes a new possibility for interpreting the observed features of Es, i.e., the "summer anomaly".

Among the atoms/ions in the metal layers, sodium atoms were first and widely detected by lidars. The sporadic sodium layer (SSL) has attracted researchers' attention for many years. Dou et al. (2009b, 2010a) statistically studied the relationship of the SSL, Es and the meteor input over the mid-latitude region, using the observations from ground-based sodium ldiar, meteor radar and satellite occultation. They found that the seasonal variation of the meteor input number showed a maximum during summer and a minimum during winter, which correlated well with the seasonal occurrence of SSL and Es. From a statistical point of view, a meteor-Es-SSL chain could be a reasonable interpretation. This interpretation is briefly described as following: assuming the incoming meteors are the source of the Es and the SSL, the metal ions are converged into Es layer by the wind shear related with atmospheric waves, and follow the downward phase progression of the waves to form SSL upon recombination.

In actuality, SSLs have been observed in a different latitude region. Figure 3 shows four SSLs observed by sodium lidars of the Chinese Meridian Project and located in Beijing, Hefei, Wuhan and Haikou, respectively. Using these four lidars together with three ionosondes located in Beijing, Wuhan and Haikou, Dou et al. (2013) studied the latitudinal distribution and correlation of SSL and Es. The SSLs at four lidar sites showed evidence of summer enhancements, and they correlated well with Es. The co-observations of SSLs at three lidar site pairs, i.e., Hefei-Beijing, Hefei-Wuhan, and Hefei-Haikou, indicated that a large-scale SSL extended horizontally for at least a few hundred kilometers. Moreover, the SSLs were better correlated in the Hefei-Wuhan and Hefei-Haikou pairs than in the Hefei-Beijing pair, which suggested a difference in the dynamical/chemical process in the MLT between the Beijing and the other sites.

The recent observations showed that the upside of the metal layer was able to extend to the thermospheric region of 120–170 km (Höffner and Friedman, 2004, 2005; Chu et al., 2011; Friedman et al., 2013). Gong et al. (2003) reported

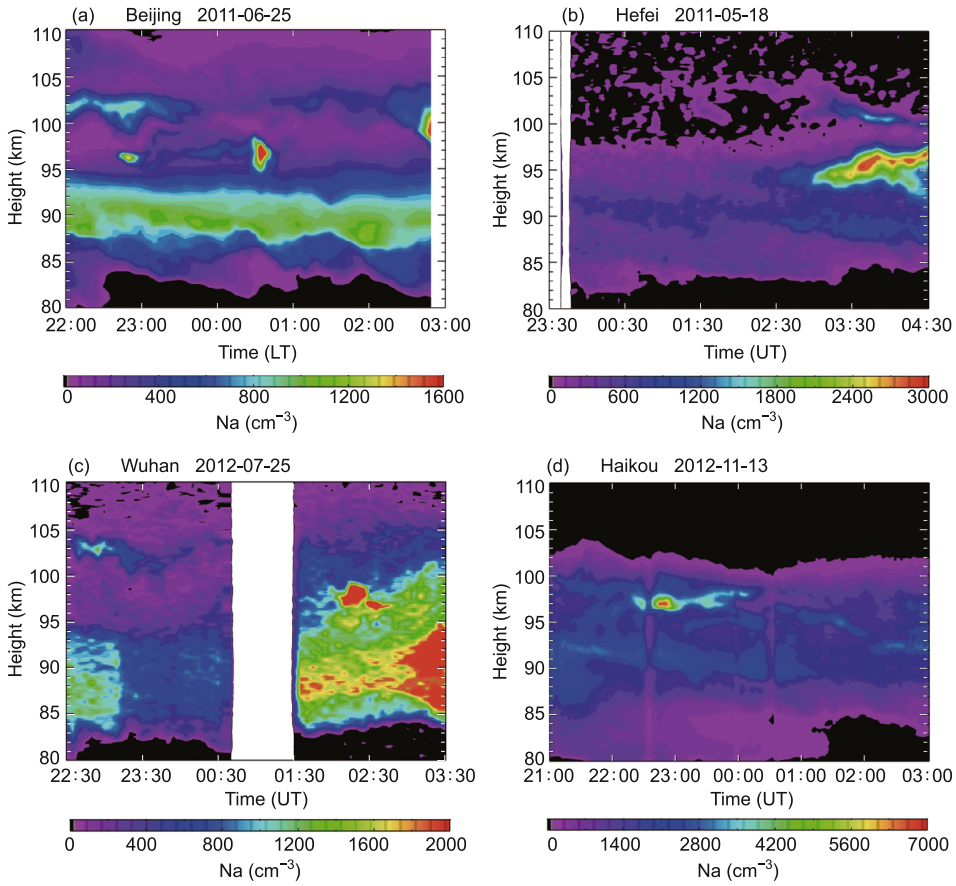

Figure 3 The SSLs observed by sodium lidars located at Beijing (a), Hefei (b), Wuhan (c), and Haikou (d), respectively. Adopted from Dou et al. (2013).

a case of a thermospheric sodium layer (also called a double sodium layer by the authors) in Wuhan using a sodium lidar. Wang et al. (2012) statistically studied 17 thermospheric sodium layers observed through a sodium lidar located in Beijing over the observations of 300 nights. They illustrated that the thermospheric sodium layers frequently occurred during spring and summer when the altitude region was distributed from 105–130 km. Recently, Xue et al. (2013) reported two thermospheric sodium layers at a low- latitude station in Lijiang. With the help of the adjacent ground-based and space-borne ionospheric radio observations, they suggested that the formation of the thermospheric sodium layers was related to an "Es-Thermospheric sodium layer" chain formed through the tidal wind shear mechanism, as is shown in Figure 4.

Besides the sodium layer, the detection of the other metal atoms/ions is also an attractive topic. Yi et al. (2013) reported common-volume observations of sporadic metal layers in the MLT region through three lidars. The sporadic layering events of Na, Fe and Ca (Ca^+) can be observed simultaneously. The altitudes of all the sporadic metal atoms/ions agreed with each other, and the evaluation of these layers followed almost the same track. The results indicated that the sporadic metal layers are usually a mixture of multiple metal atoms and ions and suggested that all these metal species in a mixture were the product of the same or similar source processes.

Various numerical models associated with metal layers or sporadic metal layers have been developed, which have been coupled with photo-chemistry or dynamics (Collions et al., 2002, Plane, 2004). Recently, some metal layer models have been successively incorporated into the atmospheric general circulation model, i.e., WACCM developed by NCAR, to study the global variation of the metal layers (Feng et al., 2013, Marsh et al., 2013). Xu and Smith (2003, 2005) calculated the chemical lifetime of the sodium from the eigenvalues and eigenvectors of the sodium chemical system. They found that the lifetime is much longer in the vicinity of the mesospheric sodium layer and verified that the sodium could be deemed as a positive tracer for the atmospheric dynamical process (e.g., gravity waves). Xu et al. (2006b) developed a nonlinear model of the sodium layer, which is time-dependent, two-dimensional, nonlinear, and non-hydrostatic (Xu et al. 2003), to study the effect of gravity waves on the sodium layer. They found that the model and observations showed similar behavior in the evolution of the sodium densities, mixing ratios, and potential temperature in response to large- and small-scale waves. Based on the theoretical study of the sodium photon-chemistry. Xu et al. (2005) also proposed a new retrieval method for satellite

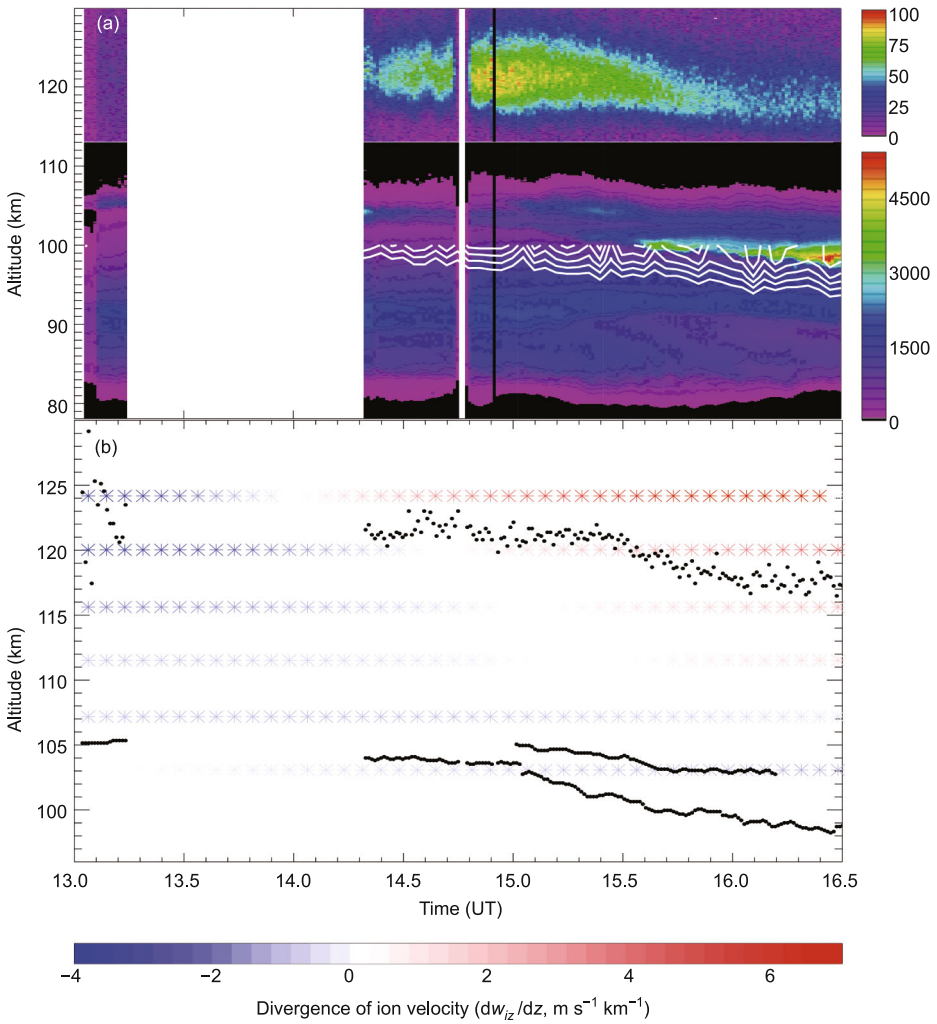

Figure 4 (a) The development of the whole sodium layer during the observational period 13:00 UT–16:30 UT on 10 March 2012, at Lijiang, China. Above 110 km, an evident thermospheric sodium layer appeared, and then decayed gradually. However, the SSL in the main layer below was enhanced and reached its maximum at the end of the observation. The blank area is due to the thin cloud covering over the lidar site. The MF received power is contoured as the solid white lines; the contour levels are 10000 to 30000 in the arbitrary unit, with an interval of 5000. (b) The calculated divergence of the ion vertical motion on 10 March 2012. The negative divergence is represented by blue; the positive, red. The peak height of the thermospheric sodium layer and the SSL versus time are represented by the black dots. In an ion-convergent region, the thermospheric sodium layer (or SSL) can be enhanced, while in an ion-divergent region, the layer density tends to decrease. Adopted from Xue et al. (2013).

remote sensing of global sodium during the nighttime through the use of satellite limb observations of ozone density, neutral temperature and Na nightglow volume emission rate.

4 The coupling of atmospheric tides and the ionospheric F2-layer

Atmospheric waves transform the energy from the lower atmosphere to the upper atmosphere and ionosphere, and play important roles in the ionosphere-thermosphere coupling. Among these atmospheric waves, the tide regularly and diurnally occurs and therefore plays an important role in the vertical propagation of atmospheric energy.

In the research on the coupling between the atmospheric tide and the ionospheric F2-region, the main challenge is that both the ionosphere and the migrating tide, which is the dominant tidal mode, have sun-synchronous diurnal variation. Thus, it is very difficult to separate the influence of the migrating tide from the ionospheric diurnal variation. On the other hand, the non-migrating tide is not sun-synchronous, and its influence is easier to separate. For example, previous research suggested that the atmospheric tide of the non-migrating tidal mode DE3 (diurnal eastward wave number 3) is the origin of the ionospheric longitudinal structure of wave number 4 (WN4), which was first observed in 2005 (Sagawa et al., 2005; Immel et al., 2006). WN4 is an important phenomenon of the ionosphere-thermosphere coupling, and can reveal the complex coupled mechanisms between the ionosphere and thermosphere. Hence, this new ionospheric distribution has attracted considerable attention.

In earlier research, it was difficult to study the WN4 climatology and diurnal variation because of the coverage limitation of the satellite observation. Wan et al. (2008) studied the seasonal and solar cycle variations of the ionospheric WN4 by using the long-term TEC data from global ionospheric maps (GIMs). As shown in Figure 5, they found that the intensity of the WN4 greatly depends on the season and, to a lesser extent, solar activity. In other words, the WN4 waves are intense and well developed in boreal summer and early boreal autumn, but quite weak in boreal winter; the intensity of the WN4 increases slightly with the increase of solar activity. Wan et al. (2008) also found that the WN4 patterns shift eastward, and the shifting speed, which is smaller in the daytime than at night, is about 90°/day in the LT-frame. This is attributed to both the eastward propagation of the DE3 in the E-region and the zonal E×B ion drifts in the F-region.

To demonstrate that the ionospheric WN4 is driven by the DE3 tide, Wan et al. (2010) studied the correlation between the above WN4 structure in the ionospheric TEC and the DE3 tidal wind in TIDI/TIMED observations. They found that the observed WN4 wave and DE3 zonal wind components experience very similar annual and inter-annual variations, and that the correlation coefficient is higher than 90%. However, the DE3 meridional wind component shows quite different behavior. Wan et al. (2010) suggested that such different correlations are attributed to the different hemispheric symmetry of different DE3 wind components. The DE3 zonal wind is likely in hemispheric symmetrical mode; hence, it can efficiently affect the ion drifts in the F-region. In contrast, the meridional wind is mainly in anti-symmetrical mode and seldom affects the ionospheric drifts.

Previous research suggested that the ionospheric vertical drifts play an important role in the coupling between the DE3 and WN4. Ren et al. (2009a) studied the diurnal and intra-annual variation of the WN4 in the equatorial vertical E×B drifts based on ROCSAT-1 observations, and found that its intra-annual variation agrees with that of the ionospheric

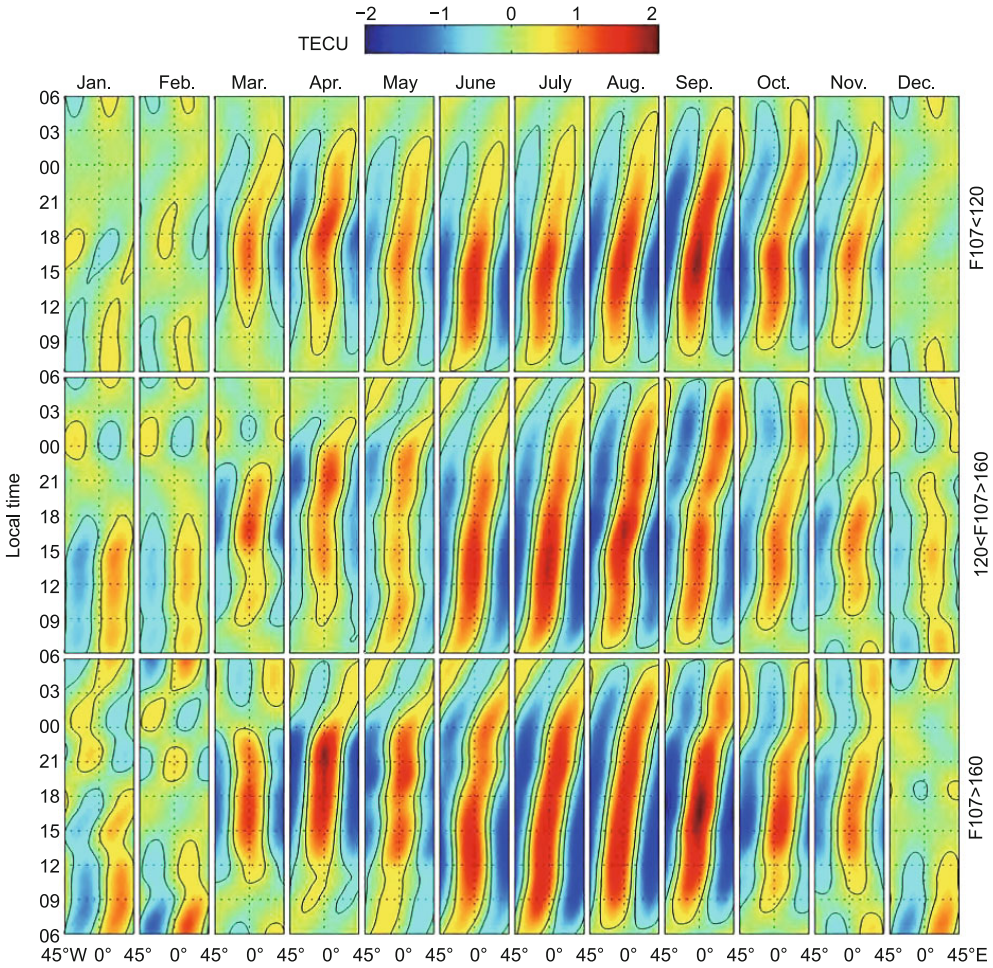

Figure 5 Patterns of the wavenumber-4 component filtered from the latitudinal integrated TEC (ITEC) of JPL GIMs. The three rows from top to bottom are for low (F107<120), medium (120<F107<160) and high (F107>160) levels of solar flux, respectively. The columns from left to right are for months January through December, respectively. Because of the recurrence of the wave patterns in the longitude domain, the figure shows only one-pattern ITEC maps in a longitude range from 45°W to 45°E. Adopted from Wan et al. (2008).

WN4 observed by Wan et al. (2008). Ren et al. (2009a) also found that the intra-annual variation of the WN4 in daytime vertical drifts agree with that of the DE3 zonal wind and temperature components. With an ionospheric dynamo model, Ren et al. (2010) simulated the WN4 in vertical drifts and found similar intra-annual variation and phase shifts. The results of Ren et al. (2010) also demonstrated what Wan et al. (2010) had suggested: the symmetrical tide can efficiently affect the F-region ion drifts, while the anti-symmetric mode could not.

Recent research suggested that the DE3 tide can also directly penetrate the thermosphere and ionosphere and drive the WN4 structure there. Ren et al. (2011a) simulated the influence of non-migrating tides on the longitudinal variations in the equinoctial lower thermosphere nitric oxide (NO), and found that DE3 tides drive the WN4 structure in the NO density and the DE2 tides (diurnal eastward wave number 2) drive the WN3, the longitudinal structure of wave number 3. They pointed out that the non-migrating tides mainly affect the longitudinal variations of the ionosphere through the modulation of the NO chemical production rate. Ren et al. (2012a) also simulated the influence of non-migrating tides on the longitudinal variations in E-region's electron density and found similar results. Wan et al. (2012) investigated the above two mechanisms with a coupled ionosphere-thermosphere model and found that the thermospheric WN4 waves are directly produced by the wave propagation mechanism; they are also indirectly created by the mechanism of electro-dynamical coupling combined with ion-neutral collision. Correspondingly, the ionospheric WN4 waves are directly produced by the electrodynamical coupling, and they can also be indirectly excited by the mechanisms of upward wave propagation combined with neutral-ion collision.

Based on the DMSP F13 satellite observations, Ren et al. (2008) also found the WN4 in the electron temperature and electron density in the sunset (17:45LT) equatorial topside ionosphere. Liu L B et al. (2008, 2009, 2010a) collected the ionospheric electron density profiles from the COSMIC radio occultation measurements and found the WN4 in ionospheric seasonal harmonics, topside ionospheric scale heights, the thickness parameter B0 and the shape parameter B1 in the IRI model. Zhao et al. (2011a, 2011b) and Li G Z (2008) found also the WN4 structure in the occurrence of F3-layer and ionospheric bubble, From the TIMED/GUVI observations, He et al. (2010) found the WN4 in the thermospheric O/N_2 column density ratio. Mu et al. (2010) also studied the correlation between the ionospheric WN3 and DE2.

The atmospheric tide affects not only the ionospheric and thermospheric structures but also their seasonal variations. Ren et al. (2011b) studied the equinoctial asymmetry of the ionospheric vertical E×B plasma drift velocity based on ROCSAT-1 observations, and the observed asymmetry exhibits obvious local time and longitude dependence. Ren et al. (2011b) simulated the effect of the drift asymmetry on the ionospheric plasma density and found that the daytime drift asymmetry can partly explain the equinoctial asymmetry in daytime low-latitude ionospheric plasma density, as observed by Liu et al. (2010b). Ren et al. (2012b) simulated alsothe influence of the lower thermospheric tidal winds on the equinoctial asymmetry of the equatorial vertical E×B plasma drifts using TIDM-IGGCAS-II model, and found the asymmetry is mainly driven by the migrating tides DW1 (diurnal) and SW2 (semidiurnal tide), as well as the non-migrating tides DE3 and DW2. Lei et al. (2011, 2013) explored the influence of the lower atmospheric tides on the latitudinal structure of the lower thermosphere and their contribution to the annual asymmetry of the upper thermosphere. Luan et al. (2012) reported the latitudinal, seasonal and solar cycle variations of terdiurnal migrating tide signatures in theionospheric TEC based on the JPL global ionospheric maps (GIMs) between 1999 and 2011. The absolute amplitude of TW3 exhibits maximum values in the magnetic equatorial region, which reaches about 8 TECU under high solar activity and 1.5 TECU under low solar activity.

Xiong et al. (2013) studied the influence of sudden stratospheric warming (SSW) in the winter of 2008/2009 on the ionosphere based on the TEC observations in Beijing, and found the enhancement in semidiurnal variation of the ionospheric TEC with a phase shift forward. They used the winds observed by an all-sky meteor radar in the same observatory to study mesospheric variation. They also found that the coupling between the mesosphere and ionosphere contributes to the semidiurnal variation of the TEC through both solar and semidiurnal lunar tides, and the enhancement in semidiurnal lunar tide is responsible for the TEC peak shift forward during the SSW. Mo et al. (2014) studied the morphology of the ionospheric equatorial anomaly during the SSW in 2005–2006.

5 Coupling between the ionosphere and the thermosphere

The collision between the charged plasma and the neutral gas is one of the fundamental processes in the upper atmosphere, and this results in the interaction and modulation of the ionosphere and the thermosphere and the variability of the upper atmosphere.

As we know, the background thermospheric winds can transport the plasma by the wind component parallel to the magnetic field lines through the ion-neutral collisions. The equatorward winds tend to move the plasma into higher altitudes where the recombination rate is lower, which causes an increase of electron density in the F-region, and vice versa. Meanwhile, the variations of zonal winds, along with the magnetic field decline effect, can also have a wind component along the magnetic field lines to further modu-

late the variation of the ionosphere. This includes the formation of the ionospheric density anomaly in the middle latitudes, which has attracted great interest of scientists in recent years. For instance, He et al. (2009) found that the change of peak electron density (NmF2) over the Weddell Sea Anomaly (WSA) is associated with the change in peak height (hmF2), while the latter is correlated closely with the components of the geomagnetic field. This indicated that the WSA is a manifestation, with a particular geometry of the magnetic field, of the evening enhancement induced by the winds. Simulations by Ren et al. (2012c) revealed that the middle latitude summer nighttime anomaly mainly appears in three distinct regions—East Asia, northern Atlantic-Europe and the South Pacific, which are mainly associated with the longitudinal variations of thermospheric zonal and meridional winds. Zhao et al. (2013) provided evidence of the longitudinal change supporting the thermospheric zonal wind mechanism by examining the climatology of NmF2 and electron density at different altitudes in the Far East regions with a longitude separation of up to 40°–60°. As shown in Figure 6, in the Far East area the daytime electron densities are higher in the West than those in the East, while at night the situation is the opposite. In addition, the daytime hmF2 in the West is higher by 30–50 km than in the East. They also suggested that the observed longitudinal variations of electron density in the Far East are associated with neutral winds and magnetic decline angle.

Based on measurements of a ground-based GPS station network, Xu J S et al. (2014) examined differences of the mid-latitude ionospheric TEC in the east and west regions of North America, South America and Oceania. Their analysis showed that the longitude variations of both declination and zonal thermospheric winds are one of the most important causes of the differences of the mid-latitude ionospheric TEC on both sides of the longitudes with zero declination. Luan and Dou (2013) studied the longitudinal and seasonal variations of the nighttime NmF2 and the corresponding hmF2 at southern middle latitudes. They found that the seasonal-local time patterns of the electron density longitudinal variations during nighttime at southern middle latitudes cannot simply be explained in terms of WSA. Besides the magnetic declination-zonal wind effects, the geographic meridional wind and the magnetic inclination also have significant effects on the upward plasma drifts and the resultant electron density.

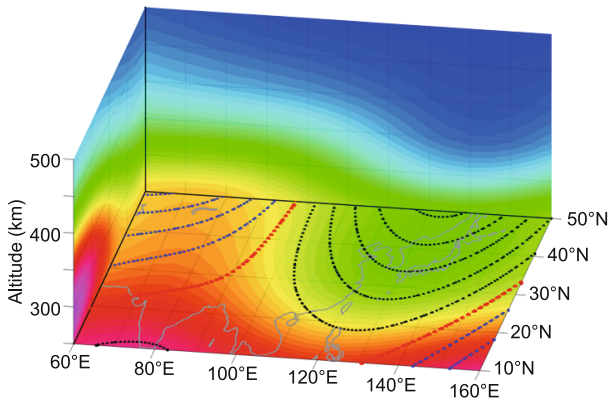

Figure 6 Three-dimensional distribution of electron densities in the Far East Asia area in the summer of 2007–2008. The variation of the magnetic decline angle (dashed line) is also included in this plot. Adopted from Zhao B Q et al. (2013).

Aside from the background neutral winds, large scale gravity waves can introduce significant variability in the ionosphere. Ding et al. (2012, 2013) and Song et al. (2012) reported variations of the two-dimensional imaging of large-scale traveling ionospheric disturbances (LSTID), and also compared the differences and similarities between the Chinese and American regions regarding the propagating feature and characteristics of the LSTID. Ding et al. (2011) obtained climatology of medium-scale traveling ionospheric disturbances (MSTIDs) from observations of a dense GPS receiver array in central China. The propagation directions and the seasonal behaviors support the view that the daytime MSTIDs are the ionospheric manifestation of atmospheric gravity waves from the lower atmosphere, while a possible excitation mechanism of nighttime MSTIDs is the electro-dynamic process caused by plasma instability in the F-region. With the network observations of both GPS receivers and ionosondes, Song et al. (2013) studied seasonal variations of the ionospheric disturbances generated by the solar terminator over China. Recently Ding et al. (2014) reported ionospheric response to the shock and acoustic waves excited by the launch of the Shenzhou 10 spacecraft. Later, Ding et al. (2012, 2013) and Song et al. (2012) reported variations of the two-dimensional imaging of LSTID, and also compared the differences and similarities between the Chinese and American regions regarding the propagating feature and characteristics of the LSTID. Xu et al. (2008) conducted a study on the relationship between TEC over East Asia and the tropospheric circulation around the Qinghai-Tibet Plateau, and found a positive correlation between the day-to-day variability of the TEC and the Asian zonal circulation index. They suggested that the dynamical effect on airflow of the plateau can generate vortexes, and these vortexes may continuously excite internal gravity waves that propagate upward to the ionosphere and cause regional wave disturbances.

Li G Z et al. (2012) investigated the large-scale wave structures (LSWS) and the onset and development of the ESF over Sanya (18°N, 109°E) in 2011. Correlative studies between the LSWS and ESF activities during the observational period offer consolidated evidence that the LSWS is a necessary precursor for the ESF development. On the other hand, the appearance of the LSWS alone may not be sufficient to produce the post-sunset F-region irregularities responsible for ionospheric scintillations. Factors aside from the LSWS could play crucial roles in the growth of ESF instabilities that are responsible for ionospheric scintilla-

tions. Li G Z et al. (2013a) further revealed the frequent occurrences of multiple plumes over two stations, i.e., the Equatorial Atmosphere Radar (EAR) (0.2°S, 100.3°E; dip latitude 10.4°S) and the Sanya VHF radar (18.4°N, 109.6°E; dip latitude 12.8°N). However, for the 21 March 2012 event, the EAR measured multiple plume structures that developed successively in the radar-scanned area with east-west separation of ~50 km, with no sunset plasma plume over Sanya. Their study implied that the simultaneous occurrence of the small-scale wave structures (SSWS) and LSWS is the preferred condition for the generation of the ESF. Li G Z et al. (2013b) reported a rare observation of daytime 150 km echoes with the small Sanya VHF radar preceded by the occurrence of an unusual intermediate layer, which is identified as abnormal traces at the upper *E* region in corresponding ionograms. The abnormal intermediate layer associated with possible gravity wave activity could significantly contribute to the growth of irregularities. It is also interesting that Xiao et al. (2007), Xiao et al. (2009) and Hao et al. (2012) analyzed the ionospheric disturbances associated with typhoons and earthquakes. They attributed the observed disturbances to the upward propagation of the atmospheric gravity.

The previous sections described the recent progress of the studies in the influence of the background thermosphere on the ionosphere. The impact of the ions on the neutral gas is another interesting aspect of the ion-neutral coupling. As revealed in Lei et al. (2012a, 2012b), neither heat transport due to zonal winds nor chemical heating is able to explain the formation of the equatorial thermosphere anomaly (ETA) crests. Instead, it was found that plasma-neutral collision heating and the field-aligned ion drag are the major contributors in producing the ETA crest and trough, respectively. As shown in Figure 7, the crest- trough difference in the exosphere temperature is 46 K, and the corresponding crest-trough ratio in thermosphere density at 400 km is 1.06. Additionally, the crests of the ETA always locate poleward

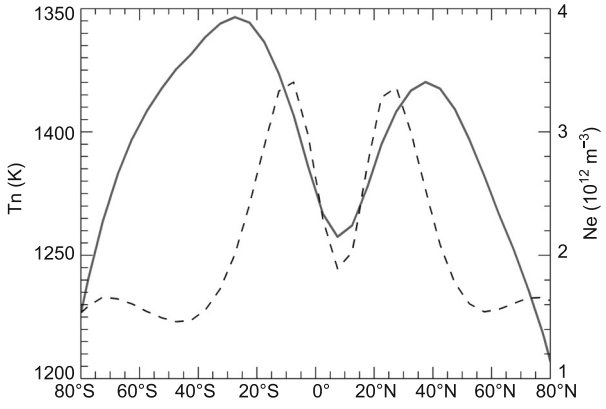

Figure 7 Latitudinal distribution of thermospheric temperature (sold line) and peak density of F2 layer (dash line, unit is 10^{12} m^{-3}) from theoretical model including the heating from field-line ion drag and ion-neutral collision. The local time and longitude are 14:00 and 110°E, respectively.

by 10°–15° with respect to those of the equatorial ionosphere anomaly (EIA) (Liu et al., 2007; Lei et al., 2010a, 2012c). It is interesting to point out that Liu et al. (2011) demonstrated a similar ETA feature observed in the nighttime thermospheric density, albeit the occurrence is lower compared with that of the daytime. Whether the formation of the nighttime ETA is also associated with the ion-neutral coupling is an interesting topic that will be explored in the future.

Beside the momentum transfer between the ions and the neutrals through ion drag, energy exchange between the ions and neutrals also affects the status of the thermosphere. Ruan et al. (2013) suggested that photoelectron heating from the conjugate summer hemisphere might be the main contributor to pre-midnight enhancement in ion temperature by the ion-neutral collisional heating, which results in a subsequent enhancement in neutral temperature in January, 2012. During storm-time, the elevated Joule heating due to the increase of particle precipitation and the associated conductivities results in significant changes of the upper thermosphere (e.g., Richmond and Lu, 2000; Lei et al, 2010b, 2012d). Xu et al. (2013a, 2013b) demonstrated that there are strong longitudinal variations of the upper atmosphere at high-latitudes over all seasons, and their simulations further confirmed that auroral heating causes the observed longitudinal variations (about 10%–20% to the zonal mean). Interestingly, the impact of auroral heating on the thermodynamics of the neutral atmosphere can penetrate down to about 105 km.

Because of the complex and highly coupled processes in thermosphere and ionosphere, simulations play an important role in the studying of the thermosphere and ionosphere, and one needs to develop complex numerical models of this coupled system. To simulate the complex and highly coupled physical and chemical processes in the ionosphere-thermosphere system, Ren et al. (2009b) developed a new global time-dependent three-dimensional coupled ionosphere-thermosphere. This model self-consistently calculates the time-dependent three-dimensional structures of the main thermospheric and ionospheric parameters in a spherical geomagnetic coordinate in the height range from 90 to 600 km, including neutral number density of major species O_2, N_2, and O and minor species $N(^2D)$, $N(^4S)$, NO, He and H; ion number densities of O^+ ,O_2^+, N_2^+, NO^+, N^+ and electron; neutral, electron and ion temperature; neutral wind vectors and ionospheric electric field. This model can reproduce the main features of the thermosphere and ionosphere, and have been used in studying the influence of thermospheric variations on the ionosphere (Ren et al., 2011a, 2012a; Wan et al., 2012).

6 Summary

The coupling between the upper atmosphere and the iono-

sphere manifests chiefly from the upward energy propagation from the low atmosphere to the ionospheric altitudes. This energy propagation reveals another important origin of the ionospheric space weather—the vertical coupling of the atmosphere-ionosphere system, which is different from the typical space weather origins, such as the solar activities or solar wind-magnetosphere-ionosphere coupling. As pointed out by Forbes et al. (2000) and Rishbeth and Mendillo (2001), the space weather origin below is of similar importance as those from the above. Therefore, the investigation on the coupling between the upper atmosphere and the ionosphere plays an important role in the space weather research.

In paper we reviewed the recent research progress on the coupling of the upper atmosphere and the ionosphere, emphasizing the works of Chinese scholars, summarized as follows:

(1) We first reviewed the observation facility of the upper atmosphere, which was recently constructed in China with the support of the Chinese Meridian Project. The upper atmospheric observations are consist with the meridian chains of the optical instruments including lidars and FP interferometers in Bejing, Hefei, Wuhan and Haikou, and radio instruments including Meteor radars and MST radars in Mohe, Bejing, Wuhan and Sanya. These instruments provide plentiful data for studying the upper atmosphere.

(2) We introduced the investigations on climatology and wave disturbances in the upper atmosphere. These works concern the seasonal and inter-annual variations of the upper atmosphere and its responses to the ENSO, QBO, AO, and SAO, as well as the propagations and dissipations of the gravity waves, tides and planetary waves in the upper atmosphere.

(3) We reviewed the studies on coupling between the upper atmosphere and the low ionosphere. These works include the coupling of the sporadic E layers and planetary waves, and the relationship among the sporadic metal layers (e.g., SSL), the meteor injection and the sporadic E layers.

(4) We also reviewed research on the coupling between atmospheric tides and the ionospheric F2 layer. This body of work revealed the seasonal and solar cycle variation of the WN4 structure in the ionosphere, as well as the correlation between the ionospheric WN4 and the non-migrating tide DE3 in the upper atmosphere. New mechanisms and models were proposed to explain the WN4-DE3 coupling process.

(5) Finally, we reviewed studies on ionosphere-thermosphere coupling. These works deal with the nighttime enhancement of the atmospheric winds, as well as the thermospheric equatorial anomaly created by the collision between the ions and neutron particles.

From the above summary, it is clear that Chinese investigators have made significant progress in the coupling between the ionosphere and upper atmosphere, and these contributions include the observation, data precession, modeling and mechanism analysis.

We would like to give the thanks to Dou XianKang, Lei JiuHou, Li Tao, Ren ZhiPeng, Xue XiangHui and Zhang ShaoDong, for their kindly discussion when preparing this review paper. This work is supported by the Chinese Academy of Sciences (Grant No. KZZD-EW-01-2), National Important Basic Research Project (Grant No. 2011CB811405) and National Natural Science Foundation of China (Grant Nos. 41131066, 41321003).

Abdu M A, Pancheva D, Bhattacharyya A. 2011. Aeronomy of the Earth's Atmosphere and Ionosphere. Heidelberg: Springer

Andrews D G, Holton J R, Leovy C B. 1987. Middle Atmosphere Dynamics. San Diego: Academic Press

Basu S, Pallamraju D. 2006. Science rationale for CAWSES (Climate and Weather of the Sun-Earth System): SCOSTEP's interdisciplinary program for 2004–2008. Adv Space Res, 38: 1781–1791

Chapman S, Lindzen R S. 1970. Atmospheric Tides. Norwell: Reidel Mass

Chen D, Chen Z Y, Lü D R. 2012. Simulation of the stratospheric gravity waves generated by the Typhoon Masta in 2005. Chin Sci Earth Sci, 55: 602–610

Chen L, Yi F. 2011. Average properties and small-scale variations of the mesospheric Na and Fe layers as observed simultaneously by two closely collocated lidars at 30°N. Ann Geophys, 29: 1037–1048

Chen Z Y, Lü D R. 2009. Global structures of the DE3 tide. Chin Sci Bull, 54: 1073–1079

Christensen A B, Walterscheid R L, Ross M N, et al. 1994. Global Ultraviolet Imager (GUVI) for the NASA Thermosphere-Ionosphere-Mesosphere Energetics and Dynamics (TIMED) mission. Proc SPIE, 2266: 451–466

Collins S C, Plane J M C, Kelley M C, et al. 2002. A study of the role of ion-molecule chemistry in the formation of sporadic sodium layers. J Atmos Sol-Terr Phy, 64: 845–860

Chu X Z, Yu Z B, Gardner C S, et al. 2011. Lidar observations of neutral Fe layers and fast gravity waves in the thermosphere (110–155 km) at McMurdo (77.8°S, 166.7°E), Antarctica. Geophys Res Lett, 38: L23807

Ding F, Wan W X, Xu G R, et al. 2011. Climatology of medium-scale traveling ionospheric disturbances observed by a GPS network in central China. J Geophys Res, 116: A09327

Ding F, Wan W X, Ning B Q, et al. 2012. Two-dimensional imaging of large-scale traveling ionospheric disturbances over China based on GPS data. J Geophys Res, 117: A08318

Ding F, Wan W X, Ning B Q, et al. 2013. Observations of poleward-propagating large-scale traveling ionospheric disturbances in southern China. Ann Geophys, 31: 377–385

Ding F, Wan W X, Mao T, et al. 2014. Ionospheric response to the shock and acoustic waves excited by the launch of the Shenzhou 10 spacecraft. Geophys Res Lett, doi: 10.1002/2014GL060107

Dou X K, Li T, Xu J Y, et al. 2009a. Seasonal oscillations of middle atmosphere temperature observed by Rayleigh lidars and their comparisons with TIMED/SABER observations. J Geophys Res, 114: D20103

Dou X K, Xue X H, Chen T D, et al. 2009b. A statistical study of sporadic sodium layer observed by sodium lidar at Hefei (31.8°N, 117.3°E). Ann Geophys, 27: 2247–2257

Dou X K, Xue X H, Li T, et al. 2010a. Possible relations between Meteors, enhanced electron density layers and sporadic sodium layers. J Geophys Res, 115: A06311

Dou X K, Li T, Tang Y H, et al. 2010b. Variability of gravity wave occurrence frequency and propagation direction in the upper mesosphere observed by the OH imager in Northern Colorado. J Atmos Sol-Terr Phy, 72: 457–462

Dou X K, Qiu S C, Xue X H, et al. 2013. Sporadic and thermospheric enhanced sodium layers observed by a lidar chain over China. J Geophys Res-Space, 118: 6627–6643

Feng W H, Marsh D R, Chipperfield M P, et al. 2013. A global atmospheric model of meteoric iron. J Geophys Res, 118: D50708

Forbes J M, Palo S E, Zhang X L. 2000. Variability of the ionosphere. J

Atmos Sol-Terr Phy, 62: 685–693
Friedman J S, Chu X, Brum C G M, et al. 2013. Observation of a thermospheric descending layer of neutral K over Arecibo. J Atmos Sol-Terr Phy, doi: 10.1016/j.jastp.2013.03.002
Fritts D C, Alexander M J. 2003. Gravity wave dynamics and effects in the middle atmosphere. Rev Geophys, 41: 1003
Gan Q, Zhang S D, Yi F. 2012. TIMED/SABER observations of lower mesospheric inversion layers at low and middle latitudes. J Geophys Res, 117: D07109
Garcia R R, Dunkerton T J, Lieberman R S, et al. 1997. Climatology of the semiannual oscillation of the tropical middle atmosphere. J Geophys Res, 102: 26019–26032
Gardner C S, Voelz D G. 1987. Lidar studies of the nighttime sodium layer over Urbana, Illinois, 2: Gravity waves. J Geophys Res, 92: 4673–4693
Gong S H, Yang G T, Xu J Y, et al. 2013. Statistical characteristics of atmospheric gravity wave in the mesopause region observed with a sodium lidar at Beijing, China. J Atmos Sol-Terr Phy, 97: 143–151
Gong S S, Zen X Z, Xue X J. 1997. First observations of sodium layer over Wuhan, China. Sci Sin Math, 40: 369–373
Gong S S, Yang G T, Wang J M, et al. 2003. A double sodium layer event observed over Wuhan China by lidar. Geophys Res Lett, 30: 1209
Gong Y, Zhou Q H. 2011. Incoherent scatter radar study of the terdiurnal tide in the E- and F-region heights at Arecibo. Geophys Res Lett, 38: L15101
Gong Y, Zhou Q H, Zhang S D. 2013. Atmospheric tides in the low latitude E- and F-region and their response to a sudden stratospheric warming in January 2010. J Geophys Res-Space, 118: 7913–7927
Gu S Y, Li T, Dou X K, et al. 2013a. Observations of quasi-two-day wave by TIMED/SABER and TIMED/TIDI. J Geophys Res-Atmos, 118: 1624–1639
Gu S Y, Li T, Dou X K, et al. 2013b. Long-term observations of the quasi two-day wave by Hawaii MF radar. J Geophys Res-Space, 118: 7886–7894
Guo J P, Wan W X, Forbes J M, et al. 2007. Effects of solar variability on thermosphere density from CHAMP accelerometer data. J Geophys Res, 112: A10308
Hao Y Q, Xiao Z, Zhang D H. 2012. Multi-instrument observation on coseismic ionospheric effects after great Tohoku earthquake. J Geophys Res, 117: A02305
He M S, Liu L B, Wan W X, et al. 2009. A study of the Weddell Sea Anomaly observed by FORMOSAT-3/COSMIC. J Geophys Res, 114: A12309
He M S, Liu L B, Wan W X, et al. 2010. Longitudinal modulation of the O/N_2 column density retrieved from TIMED/GUVI measurement. Geophys Res Lett, 37: L20108
Höffner J, Friedman J S. 2004. Metal layers at high altitudes: A possible connection to meteoroids. Atmos Chem Phys Discuss, 4: 399–417
Höffner J, Friedman J S. 2005. The mesospheric metal layer topside: Examples of simultaneous metal observations. J Atmos Sol-Terr Phy, 67: 1226–1237
Holton J R. 1982. The role of gravity wave induced drag and diffusion in the momentum budget of the mesosphere. J Atmos Sci, 39: 791–799
Holton J R, Alexander M J. 2000. The role of waves in the transport circulation of the middle atmosphere. In: Atmospheric Science Across the Stratopause. Geophys Monogr Ser, 123: 21–35
Huang C M, Zhang S D, Yi F. 2009. Intensive radiosonde observations of the diurnal tide and planetary waves in the lower atmosphere over Yichang (111°18′E, 30°42′N). Ann Geophys, 27: 1079–1095
Huang C M, Zhang S D, Zhou Q, et al. 2012. Atmospheric waves and their interactions in the thermospheric neutral wind as observed by the Arecibo incoherent scatter radar. J Geophys Res, 113: D02102
Huang C M, Zhang S D, Yi F, et al. 2013. Frequency variations of gravity waves interacting with a time-varying tide. Ann Geophys, 31: 1731–1743
Huang K M, Zhang S D, Yi F. 2009. Gravity wave excitation through resonant interaction in a compressible atmosphere. Geophys Res Lett, 36: L01803
Huang K M, Zhang S D, Yi F. 2010. Reflection and transmission of atmospheric gravity waves in a stably sheared horizontal wind field. J Geophys Res, 115: D16103
Huang K M, Liu A Z, Zhang S D, et al. 2012. Spectral energy transfer of atmospheric gravity waves through sum and difference nonlinear interactions. Ann Geophys, 30: 303–315
Huang K M, Zhang S D, Yi F, et al. 2013a. Third-order resonant interaction of atmospheric gravity waves. J Geophys Res-Atmos, 118: 2197–2206
Huang K M, Liu A Z, Lu X, et al. 2013b. Nonlinear coupling between quasi two-day wave and tides based on meteor radar observations at Maui. J Geophys Res, 118: 10936–10943
Huang K M, Liu A Z, Zhang S D, et al. 2013c. A strong nonlinear interaction event between 16-day wave and diurnal tide from meteor radar observations. Ann Geophys, 31: 2039–2048
Huang Y Y, Zhang S D, Yi F, et al. 2013. Global climatological variability of quasi-two-day waves revealed by SABER/TIMED observations. Ann Geophys, 31: 1061–1075
Immel T J, Sagawa E, England S L, et al. 2006. Control of equatorial ionospheric morphology by atmospheric tides. Geophys Res Lett, 33: L15108
Jiang G Y, Xu J Y, Xiong J, et al. 2008. A case study of the mesospheric 6.5-day wave observed by radar systems. J Geophys Res, 113: D16111
Jiang G Y, Xu J Y, Franke S J. 2009. The 8-h tide in the mesosphere and lower thermosphere over Maui (20.75ºN, 156.43ºW). Ann Geophys, 27: 1989–1999
Jiang G Y, Xu J Y, Shi J, et al. 2010. The first observation of the atmospheric tides in the mesosphere and lower thermosphere over Hainan, China. Chin Sci Bull, 55: 1059–1066
Jiang G Y, Xu J Y, Yuan W, et al. 2012. A comparison of mesospheric winds measured by FPI and meteor radar located at 40ºN. Sci China Tech Sci, 55: 1245–1250
Killeen T L, Skinner W R, Johnson R M, et al. 1999. The TIMED doppler interferometer (TIDI). Proc SPIE, 3756: 289–303
Killeen T L, Wu Q, Solomon S C, et al. 2005. TIMED Doppler interferometer: Overview and recent results. J Geophys Res, 111: A10S01
Leblanc T, McDermid I S, Keckhut P, et al. 1998. Temperature climatology of the middle atmosphere from long-term lidar measurements at middle and low latitudes. J Geophys Res, 103: 17191–17204
Lei J H, Thayer J P, Forbes J M. 2010a. Longitudinal and geomagnetic activity modulation of the equatorial thermosphere anomaly. J Geophys Res, 115: A08311
Lei J H, Thayer J P, Burns A G, et al. 2010b. Wind and temperature effects on thermosphere mass density response to the November 2004 geomagnetic storm. J Geophys Res, 115: A05303
Lei J H, Forbes J M, Liu H L, et al. 2011. Latitudinal variations of middle thermosphere: Observations and modeling. J Geophys Res, 116: A12306
Lei J H, Thayer J P, Wang W, et al. 2012a. Simulations of the equatorial thermosphere anomaly: Field-aligned ion drag effect. J Geophys Res, 117: A01304
Lei J H, Thayer J P, Wang W, et al. 2012b. Simulations of the equatorial thermosphere anomaly: Physical mechanisms for crest formation. J Geophys Res, 117: A06318
Lei J H, Matsuo T, Dou X, et al. 2012c. Annual and semiannual variations of thermospheric density: EOF analysis of CHAMP and GRACE data. J Geophys Res, 117: A01310
Lei J H, Burns A G, Thayer J P, et al. 2012d. Overcooling in the upper thermosphere during the recovery phase of the 2003 October storms. J Geophys Res, 117: A03314
Lei J H, Dou X K, Burns A G, et al. 2013. Annual asymmetry in thermospheric density: Observations and simulations. J Geophys Res-Space, 118: 2503–2510
Li G Z, Ning B Q, Liu L B, et al. 2008. Correlative study of plasma bubbles, evening equatorial ionization anomaly, and equatorial prereversal E×B drifts at solar maximum. Radio Sci, 43: RS4005
Li G Z, Ning B Q, Abdu M A, et al. 2012. Precursor signatures and evolution of post-sunset equatorial spread-F observed over Sanya. J Geophys Res, 117: A08321
Li G Z, Ning B Q, Abdu M A, et al. 2013a. Longitudinal characteristics of spread F backscatter plumes observed with the EAR and Sanya VHF

radar in Southeast Asia. J Geophys Res-Space, 118: 6544–6557
Li G Z, Ning B Q, Patra A K, et al. 2013b. On the linkage of daytime 150 km echoes and abnormal intermediate layer traces over Sanya. J Geophys Res-Space, 118: 7262–7267
Li Q, Xu J Y, Yue J, et al. 2011. Statistical characteristics of gravity wave activities observed by an OH airglow imager at Xinglong, in northern China. Ann Geophys, 29: 1401–1410
Li Q, Xu J Y, Yue J, et al. 2013. Investigation of a mesospheric bore event over northern China. Ann Geophys, 31: 409–418
Li T, She C Y, Liu H L, et al. 2007. Evidence of a gravity wave breaking event and the estimation of wave characteristics from sodium lidar observation over Fort Collins, CO (41°N, 105°W). Geophys Res Lett, 34: L05815
Li T, Leblanc T, McDermid I S. 2008. Interannual variations of middle atmospheric temperature as measured by the JPL lidar at Mauna Loa Observatory, Hawaii (19.5°N, 155.6°W). J Geophys Res, 113: D14109
Li T, She C Y, Liu H L, et al. 2009. Observation of local tidal variability and instability, along with dissipation of diurnal tidal harmonics in the mesopause region over Fort Collins, CO (41°N, 105°W). J Geophys Res, 114: D06106
Li T, Leblanc T, McDermid I S, et al. 2010. Seasonal and inter-annual variability of gravity wave activity revealed by long-term lidar observations over Mauna Loa Observatory, Hawaii. J Geophys Res, 115: D13103
Li T, Leblanc T, McDermid I S, et al. 2011. Middle atmosphere temperature trend and solar cycle revealed by long-term Rayleigh lidar observations. J Geophys Res, 116: D00P05
Li T, Fang X, Liu W, et al. 2012a. Narrowband sodium lidar for the measurements of mesopause region temperature and wind. Appl Opt, 51: 5401–5411
Li T, Liu A Z, Lu X, et al. 2012b. Meteor-radar observed mesospheric semi-annual oscillation (SAO) and quasi-biennial oscillation (QBO) over Maui, Hawaii. J Geophys Res, 117: D05130
Li T, Calvo N, Yue J, et al. 2013. Influence of El Niño-Southern Oscillation in the mesosphere. Geophys Res Lett, 40: 3292–3296
Lindzen R S. 1981. Turbulence and stress owing to gravity wave and tidal breakdown. J Geophys Res, 86: 9707–9714
Liu H L, Hagan M E. 1998. Local heating/cooling of the mesosphere due to gravity wave and tidal coupling. Geophys Res Lett, 25: 2941–2944
Liu H X, Lühr H, Watanabe S. 2007. Climatology of the equatorial thermospheric mass density anomaly. J Geophys Res, 112: A05305
Liu J, Liu L B, Zhao B Q, et al. 2011. On the relationship between the pos tmidnight thermospheric equatorial mass anomaly and equatorial ionization anomaly under geomagnetic quiet conditions. J Geophys Res, 116: A12312
Liu L B, He M S, Wan W X, et al. 2008. Topside ionospheric scale heights retrieved from Constellation Observing System for meteorology, ionosphere, and climate radio occultation measurements. J Geophys Res, 113: A10304
Liu L B, Zhao B Q, Wan W X, et al. 2009. Seasonal variations of the ionospheric electron densities retrieved from Constellation Observing System for meteorology, ionosphere, and climate mission radio occultation measurements. J Geophys Res, 114: A02302
Liu L B, Wan W X, Ning B Q, et al. 2010a. Longitudinal behaviors of the IRI-B parameters of the equatorial electron density profiles retrieved from FORMOSAT-3/COSMIC radio occultation measurements. Adv Space Res, 46: 1064–1069
Liu L B, He M S, Yue X A, et al. 2010b. Ionosphere around equinoxes during low solar activity. J Geophys Res, 115: A09307
Liu L B, Wan W X, Chen Y D, et al. 2011. Solar activity effects of the ionosphere: A brief review. Chin Sci Bull, 56: 1202–1211, doi: 10.1007/s11434-010-4226-9
Liu X, Xu J Y, Liu H L, et al. 2008. Nonlinear interactions between gravity waves with different wavelengths and diurnal tide. J Geophys Res, 113: D08112
Liu X, Xu J Y, Gao H, et al. 2009. Kelvin-Helmholtz billows and their effects on mean state duringgravity wave propagation. Ann Geophys, 27: 2789–2798
Liu X, Zhou Q H, Yuan W, et al. 2012. Influences of non-isothermal atmospheric backgrounds on variations of gravity wave parameters. Sci China Tech Sci, 55: 1251–1257
Liu X, Xu J Y, Yue J, et al. 2013. Numerical modeling study of the momentum deposition of small amplitude gravity waves in the thermosphere. Ann Geophys, 31: 1–14
Luan X L, Dou X K, Lei J H, et al. 2012. Terdiurnal migrating-tide signature in ionospheric total electron content. J Geophys Res, 117: A11302
Luan X L, Dou X K. 2013. Seasonal dependence of the longitudinal variations of nighttime ionospheric electron density and equivalent winds at southern midlatitudes. Ann Geophys, 31: 1699–1708
Ma R P, Xu J Y, Wang W B, et al. 2010. Variations of the nighttime thermospheric mass density at low and middle latitudes. J Geophys Res, 115: A12301
Marsh D R, Janches D, Feng W, et al. 2013. A global model of meteoric sodium. J Geophys Res-Atmos, 118: 11442–11452
Mo X H, Zhang D H, Goncharenko L P, et al. 2014. Quasi-16-day periodic meridional movement of the equatorial ionization anomaly. Ann Geophys, 32: 121–131, doi:10.5194/angeo-32-121-2014
Mu W F, Wan W X, Ren Z P, et al. 2010. Correlation between ionospheric longitudinal harmonic components and upper atmospheric tides. Chin Sci Bull, 55: 4037–4045
Niciejewski R J, Killeen T L, Turnbull M. 1994. Ground-based fabry-perot interferometry of the terrestrial nightglow with a bare charge-coupled device: Remote field site deployment. Opt Eng, 33: 457–465
Niu X J, Xiong J G, Wan W X, et al. 2005. Lunar tidal winds in the mesosphere over wuhan and adelaide. Adv Space Res, 36: 2218–2222
Pancheva D V, Fejer B G, Garcia R R, et al. 2006. Vertical coupling in the atmosphere/ionosphere system. J Atmos Sol-Terr Phy, 68: 245–598
Pancheva D V, Haldoupis C, Marsh D R, et al. 2007. Vertical coupling in the atmosphere/ionosphere system. J Atmos Sol-Terr Phy, 69: 2081–2522
Pancheva D, Shiokawa K, Knizova P, et al. 2012. Recent progress in the vertical coupling in the atmosphere-ionosphere system. J Atmos Sol-Terr Phy, 90-91: 1–222
Peterson A W, Kieffaber L M. 1973. Infrared photography of OH airglow structures. Nature, 242: 321–322
Peterson A W, 1979. Airglow events visible to the naked eye. Applied Optics, 18: 3390–3393
Plane J M C. 2004. A new time-resolved model of the mesospheric Na layer: Constraints on the meteor input function. Atmos Chem Phys Discuss, 4: 39–69
Reigber C, Lühr H, Schwintzer P. 2002. CHAMP mission status, Adv Space Res, 30: 129–134, doi: 10.1016/S0273-1177(02)00276-4
Ren Z P, Wan W X, Liu L B, et al. 2008. Longitudinal variations of electron temperature and total ion density in the sunset equatorial topside ionosphere. Geophys Res Lett, 35: L05108
Ren Z P, Wan W X, Liu L B, et al. 2009a. Intra-annual variation of wave number 4 structure of vertical E×B drifts in the equatorial ionosphere seen from Rocsat-1. J Geophys Res, 114: A05308
Ren Z P, Wan W X, Liu L B. 2009b. GCITEM-IGGCAS: A new global coupled ionosphere-thermosphere-electrodynamics model. J Atmos Sol-Terr Phy, 71: 2064–2076
Ren Z P, Wan W X, Xiong J G, et al. 2010. Simulated wave number 4 structure in equatorial F-region vertical plasma drifts. J Geophys Res, 115: A05301
Ren Z P, Wan W X, Liu L B. et al. 2011a. Simulated longitudinal variations in the lower thermospheric nitric oxide induced by nonmigrating tides. J Geophys Res, 116: A04301
Ren Z P, Wan W X, Liu L B. et al. 2011b. Equinoctial asymmetry of ionospheric vertical plasma drifts and its effect on F-region plasma density. J Geophys Res, 116: A02308
Ren Z P, Wan W X, Liu L B. et al. 2012a. Simulated longitudinal variations in the E-region plasma density induced by non-migrating tides. J Atmos Sol-Terr Phy, 90-91: 68–76
Ren Z P, Wan W X, Xiong J G. et al. 2012b. Simulated equinoctial asymmetry of the ionospheric vertical plasma drifts. J Geophys Res, 117: A01301
Ren Z P, Wan W X, Liu L B. et al. 2012c. Simulated midlatitude summer

nighttime anomaly in realistic geomagnetic fields. J Geophys Res, 117: A03323
Richmond A D, Lu G. 2000. Upper-atmospheric effects of magnetic storms: A brief tutorial. J Atmos Sol-Terr Phy, 62: 1115–1127
Rishbeth H. 2006. F-region links with the lower atmosphere? J Atmos Sol-Terr Phy, 68: 469–478
Rishbeth H, Mendillo M. 2001. Patterns of F2-layer variability. J Atmos Sol-Terr Phy, 63: 1661–1680
Robert F, Pfaff R F. 2012. The near-earth plasma environment. Space Sci Rev, 168: 23–112
Ruan H B, Lei J H, Dou X K, et al. 2013. Enhancements of nighttime neutral and ion temperatures in the Fregion over Millstone Hill. J Geophys Res-Space, 118: 1768–1776
Russell III J M, Mlynczak M G, Gordley L L, et al. 1999. Overview of the SABER experiment and preliminary calibration results. Proc SPIE, 3756: 277–288
Sagawa E T, Immel J, Frey H U, et al. 2005. Longitudinal structure of the equatorial anomaly in the nighttime ionosphere observed by IMAGE/FUV. J Geophys Res, 110: A11302
Schmieder B, Vincent B, Baumjohann W, et al. 2004. Climate and weather of the sun-earth system: Cawses. Adv Space Res, 34: 443–448
She C Y, Yu J R, Latifi H, et al. 1992. High-spectral-resolution fluorescence light detection and ranging for mesospheric sodium temperature measurements. Appl optics, 31: 2095–2106
Shu Z F, Dou X K, Xia H Y, et al. 2012. Low stratospheric wind measurement using mobile rayleigh doppler wind lidar. J Opt Soc Korea, 16: 141–144
Song Q, Ding F, Wan W X, et al. 2012. Global propagation features of large-scale traveling ionospheric disturbances during the magnetic storm of 7–10 November 2004. Ann Geophys, 30: 683–694
Song Q, Ding F, Wan W X, et al. 2013. Statistical study of large-scale traveling ionospheric disturbances generated by the solar terminator over China. J Geophys Res Space Physics, 118: 4583–4593
Sutton E K, Nerem R S, Forbes J M. 2007. Density and winds in the thermosphere deduced from accelerometer data. J Spacecraft Rockets, 44: 1210–1219
Tang Y H, Dou X K, Li T, et al. 2014. Gravity wave characteristics in the mesopause region revealed from OH airglow imager observations over Northern Colorado. J Geophys Res-Space Physics, 119: 630–645, doi:10.1002/2013JA018955
Taylor M J. 1997. A review of advances in imaging techniques for measuring short period gravity waves in the mesosphere and lower thermosphere. Adv Space Res, 19: 667–676
Tu C, Hu X, Yan Z A, et al. 2009. First imaging observation of the gravity waves in the mesopause region in China. Chin Sci Bull, 55: 539–543
Wan W X, Liu L B, Pi X Q, et al. 2008. Wavenumber-4 patterns of the total electron content over the low latitude ionosphere. Geophys Res Lett, 35: L12104
Wan W X, Xiong J, Ren Z P, et al. 2010. Correlation between the ionospheric WN4 signature and the upper atmospheric DE3 tide. J Geophys Res, 115: A11303
Wan W X, Ren Z P, Ding F. et al. 2012. A simulation study for the couplings between DE3 tide and longitudinal WN4 structure in the thermosphere and ionosphere. J Atmos Sol-Terr Phy, 90-91: 52–60
Wang J H, Yang Y, Cheng X W, et al. 2012. Double sodium layers observation over Beijing, China. Geophys Res Lett, 39: L15801
Wu Q, Gablehouse D, Solomon S C, et al. 2004. A new Fabry-Perot interferometer for upper atmospheric research. Proc SPIE, 5660: 218–227
Wu Y F, Xu J Y. 2006. Comparison of horizontal velocity spectra derived from chaff rockets with saturation models. J Geophys Res, 111: D13109
Xia H Y, Dou X K, Sun D S, et al. 2012. Mid-altitude wind measurements with mobile rayleigh doppler lidar incorporating system-level optical frequency control method. Opt Express, 20: 15286–15300
Xiao Z, Xiao S G, Hao Y Q, et al. 2007. Morphological features of ionospheric response to typhoon. J Geophys Res, 112: A04304
Xiao S G, Xiao Z, Shi J K, et al. 2009. Observational facts in revealing a close relation between acoustic-gravity waves and midlatitude spread *F*. J Geophys Res, 114: A01303
Xiong J G, Wan W X, Ning B Q, et al. 2004. First results of the tidal structure in the MLT revealed by Wuhan meteor radar (30°40′N, 114°30′E). J Atmos Sol-Terr Phy, 66: 675–682
Xiong J G, Wan W X, Ding F, et al. 2013. Coupling between mesosphere and ionosphere over Beijing through semidiurnal tides during the 2009 sudden stratospheric warming. J Geophys Res-Space, 118: 2511–2521
Xu G R, Wan W X, She C L, et al. 2008. The relationship between ionospheric total electron content (TEC) over East Asia and the tropospheric circulation around the Qinghai-Tibet Plateau obtained with a partial correlation method. Adv Space Res, 42: 219–223
Xu J Y, Smith A K. 2003. Perturbations of the sodium layer: Controlled by chemistry or dynamics? Geophys Res Lett, 30: 2056, doi:10.1029/2003GL018040
Xu J Y, Smith A K, Ma R. 2003. A numerical study of the effect of gravity-wave propagation on minor species distributions in the mesopause region. J Geophys Res, 108: 4119
Xu J Y, Smith A K. 2005. Evaluation of processes that affect the photochemical timescale of the sodium layer. J Atmos Sol-Terr Phy, 67: 1216–1225
Xu J Y, Smith A K, Wu Q. 2005. A retrieval algorithm for satellite remote sensing of the nighttime global distribution of the sodium layer. J Atmos Sol-Terr Phy, 67: 739–748
Xu J Y, She C Y, Yuan W, et al. 2006a. Comparison between the temperature measurements by TIMED/SABER and lidar in the midlatitude. J Geophys Res, 111: A10S09
Xu J Y, Smith A K, Collins R L, et al. 2006b. Signature of an overturning gravity wave in the mesospheric sodium layer: Comparison of a nonlinear photochemical-dynamical model and lidar observations. J Geophys Res, 111: D17301
Xu J Y, Liu H L, Yuan W, et al. 2007a. Mesopause structure from termosphere, ionosphere, mesosphere, energetics, and dynamics (TIMED)/sounding of the atmosphere using broadband emission radiometry (SABER) observations. J Geophys Res, 112: D09102
Xu J Y, Smith A K, Yuan W, et al. 2007b. Global structure and long-term variations of zonal mean temperature observed by TIMED/SABER. J Geophys Res, 112: D24106
Xu J Y, Smith A K, Liu H L, et al. 2009a. Seasonal and quasi-biennial variations in the migrating diurnal tide observed by thermosphere, ionosphere, mesosphere, energetics and dynamics (TIMED). J Geophys Res, 114: D13107
Xu J Y, Smith A K, Liu H L, et al. 2009b. Estimation of the equivalent rayleigh friction in mesosphere/lower thermosphere region from the migrating diurnal tides observed by TIMED. J Geophys Res, 114: D23103
Xu J Y, Smith A K, Jiang G Y, et al. 2010a. Seasonal variation of the hough modes of the diurnal component of ozone heating evaluated from aura microwave limb sounder observations. J Geophys Res, 115: D10110
Xu J Y, Smith A K, Jiang G Y, et al. 2010b. Strong longitudinal variations in the OH nightglow. Geophys Res Lett, 37: L21801
Xu J Y, Smith A K, Jiang G Y, et al. 2012a. Features of the seasonal variation of the semidiurnal, terdiurnal and 6-h components of ozone heating evaluated from Aura/MLS observations. Ann Geophys, 30: 259–281
Xu J Y, Gao H, Smith A K, et al. 2012b. Using TIMED/SABER nightglow observations to investigate hydroxyl emission mechanisms in the mesopause region. J Geophys Res, 117: D02301
Xu J Y, Wang W B, Gao H. 2013a. The longitudinal variation of the daily mean thermospheric mass density. J Geophys Res-Space, 118: 515–523
Xu J Y, Smith A K, Wang W B, et al. 2013b. An observational and theoretical study of the longitudinal variation in neutral temperature induced by aurora heating in the lower thermosphere. J Geophys Res-Space, 118: 7410–7425
Xu J Y, Smith A K, Liu M H, et al. 2014. Evidence for nonmigrating tides produced by the interaction between tides and stationary planetary waves in the stratosphere and lower mesosphere. J Geophys Res-Atmos, 119: 471–489
Xu J S, Li X J, Liu Y W, et al. 2014. TEC differences for the mid-latitude ionosphere in both sides of the longitudes with zero declination. Adv

Space Res, doi: dx.doi.org/10.1016/j.asr.2013.01.010
Xue X H, Wan W X, Xiong J G, et al. 2007. Diurnal tides in mesosphere/low-thermosphere during 2002 at Wuhan (30.6°N, 114.4°E) using canonical correlation analysis. J Geophys Res, 112: D06104
Xue X H, Wan W X, Xiong J G, et al. 2008. The characteristics of the semi-diurnal tides in mesosphere/low-thermosphere (MLT) during 2002 at Wuhan (30.6°N, 114.4°E)—Using canonical correlation analysis technique. Adv Space Res, 41: 1415–1422
Xue X H, Dou X K, Lei J H, et al. 2013. Lower thermospheric-enhanced sodium layers observed at low latitude and possible formation: Case studies. J Geophys Res-Space, 118: 2409–2418
Yee J H, Cameron G E, Kusnierkiewicz D Y. 1999. Overview of TIMED. Proc SPIE, 3756: 244–254
Yi F, Zhang S D, Yue X C, et al. 2008. Some ubiquitous features of the mesospheric Fe and Na layer borders from simultaneous and common-volume Fe and Na lidar observations. J Geophys Res, 113: A04S91
Yi F, Yu C M, Zhang S D, et al. 2009. Seasonal variations of the nocturnal mesospheric Na and Fe layers at 30°N. J Geophys Res, 114: D01301
Yi F, Zhang S D, Yu C M, et al. 2013. Simultaneous and common-volume three-lidar observations of sporadic metal layers in the mesopause region. J Atmos Sol-Terr Phy, 102: 172–184
Yu J R, She C Y. 1993. Lidar-observed temperature structures and gravity-wave perturbations of the mesopause region in the springs of 1990–1992 over Fort Collins, CO. Appl Phys B-Photo, 57: 231–238
Yu Y, Wan W X, Ning B Q, et al. 2013. Tidal wind mapping from observations of a meteor radar chain in december 2011. J Geophys Res-Space, 118: 2321–2332
Yuan W H, Xu J Y, Ma R P, et al. 2010. First observation of mesospheric and thermospheric winds by a Fabry-Perot interferometer in China. Chin Sci Bull, 55: 4046–4051
Yuan W, Liu X, Xu J Y, et al. 2013. FPI observations of nighttime mesospheric and thermospheric winds in China and their comparisons with HWM07. Ann Geophys, 31: 1365–1378
Zhang S D, Yi F, Huang C M, et al. 2010. Latitudinal and seasonal variations of lower atmospheric inertial gravity wave energy revealed by US radiosonde data. Ann Geophys, 28: 1065–1074
Zhang S D, Yi F, Huang C M, et al. 2012. High vertical resolution analyses of gravity waves and turbulence at a midlatitude station. J Geophys Res, 117: D02103
Zhang S D, Yi F, Huang C M, et al. 2013. Latitudinal and altitudinal variability of lower atmospheric inertial gravity waves revealed by U.S. radiosonde data. J Geophys Res-Atmos, 118: 7750–7764
Zhang Y, Xiong J G, Liu L B, et al. 2012. A global morphology of gravity wave activity in the stratosphere revealed by the 8-year SABER/TIMED data. J Geophys Res, 117: D21101, doi:10.1029/2012JD017676
Zhao B Q, Wan W X, Liu L B, et al. 2008. Anomalous enhancement of ionospheric electron content in the Asian-Australian region during a geomagnetically quiet day. J Geophys Res, 113: A11302
Zhao B Q, Wan W X, Reinisch B, et al. 2011a. Features of the F3 layer in the low-latitude ionosphere at sunset. J Geophys Res, 116: A01313
Zhao B Q, Wan W X, Yue X A, et al. 2011b. Global characteristics of occurrence of an additional layer in the ionosphere observed by COSMIC/FORMOSAT-3. Geophys Res Lett, 38: L02101
Zhao B Q, Wang M, Wang Y G, et al. 2013. East-west differences inf-region electron density at midlatitude: Evidence from the far east region. J Geophys Res-Space, 118: 542–553
Zhao G X, Liu L B, Ning B Q, et al. 2005a. The terdiurnal tide in the mesosphere and lower thermosphere over wuhan (30°N, 114°E). Earth Planets Space, 57: 393–398
Zhao G X, Liu L B, Wan W X, et al. 2005b. Seasonal behavior of meteor radar winds over wuhan. Earth Planets Space, 57: 61–70
Zhao L, Chen J S, Ding Z H, et al. 2012. First observations of tidal oscillations by an MF radar over Kunming (25.6°N 103.8°E). J Atmos Sol-Terr Phy, 78-79: 44–52
Zhu Y J, Xu J Y, Yuan W, et al. 2012. First experiment of spectrometric observation of hydroxyl emission and rotational temperature in the mesopause in China. Sci China Tech Sci, 55: 1312–1318
Zuo X M, Wan W X. 2008. Planetary wave oscillations in sporadic E layer occurrence at Wuhan. Earth Planets Space, 60: 647–652
Zuo X M, Wan W X, Zhao G X. 2009. An attempt to infer information on planetary wave by analyzing sporadic E layers observations. Earth Planets Space, 61: 1185–1190